Computer Methods in Applied Mechanics and Engineering 451 (2026) 118651

Contents lists available at ScienceDirect

Comput. Methods Appl. Mech. Engrg.

journal homepage: www.elsevier.com/locate/cma

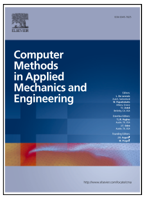

Numerical and physical robustness with respect to nodewise geometrical uncertainty in topology optimization

Justus Karnath [a,*], Benedikt Kriegesmann [a], Claus B.W. Pedersen [b]

[a] *Institute for Structural Mechanics in Lightweight Design, Hamburg University of Technology, Hamburg, Germany*
[b] *Dassault Systemes Deutschland GmbH, SIMULIA, Hamburg, Germany*

ARTICLE INFO

Keywords:
Robust design optimization
Robust topology optimization
First-order perturbation approach
Numerical mesh-dependence
Geometrical perturbations

ABSTRACT

Deterministic optimization applied to non-parametric optimization, such as topology, sizing, or shape optimization, may result in optimized designs that are highly mesh-dependent or correspond to a local minimum. Previous robust design optimization methods that consider global geometrical perturbations demonstrate the ability to suppress many local minima in the response function, and thereby, yield improved optimized designs. However, different mesh discretizations sometimes yield fundamentally different optimized designs that cannot be suppressed using global uncertainty formulations. Hence, a novel uncertainty measure is proposed, based on nodewise uncorrelated local geometric distributions. Firstly, the proposed approach employs a computationally efficient generalized first-order method, ensuring improved numerical mesh-independence of optimized designs. Secondly, the proposed method allows for a semi-intrusive implementation independent of the number of design variables and the design variable type. The proposed method is applied as a local uncertainty measure to various numerical examples addressing both numerical and physical geometrical robustness including the design of compliant hinge mechanisms, as well as stiffness- and stress-based optimization formulations.

1. Introduction

Deterministic optimization may yield structurally optimized designs that are very sensitive to even small geometrical imperfections in certain regions of the design. Therefore, minor modifications of the model caused by, e.g., manufacturing uncertainty, material uncertainty, or uncertainty with respect to the numerical discretization can cause significant reductions in structural performance. Furthermore, gradient-based optimization algorithms normally yield solutions corresponding to a local minimum. Obtaining a local minimum in topology optimization is generally a well-known phenomenon [1]. Hence, the present work aims on suppressing some of the local minima solutions by applying traditional robustness methods customized to model the uncertainty associated with different numerical discretizations. Therefore, the local minima are classified as either physical or numerical (mesh-induced).

Papadopoulos et al. [2] show that even simple optimization problems may yield highly non-convex response functions having physical mesh-independent local minima.

In contrast, numerical local minima can occur by minor geometrical differences in the numerical discretization. Talischi et al. [3] and [4] show that structured meshes can affect optimized designs by introducing favorable directions in the mesh for which the design features align with in the optimized solution. Hence, they apply unstructured polygonal meshes to prevent the mesh from affecting the optimized designs. Additionally, polygonal meshes show no checkerboarding and cannot form single-node connections. However,

---

[*] Corresponding author.
E-mail address: justus.karnath@tuhh.de (J. Karnath).

https://doi.org/10.1016/j.cma.2025.118651
Received 5 May 2025; Received in revised form 23 October 2025; Accepted 3 December 2025

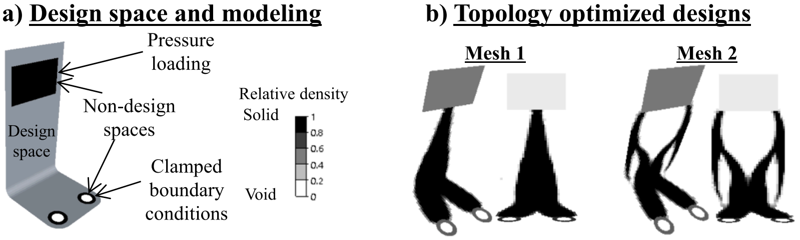

Fig. 1. (a) L-shape example and (b) deterministic topology optimized designs using two very similar finite element meshes as being investigated in Section 5.

polygonal meshes are not commonly used and are not widely available in finite element implementations. Generally, regularization is required for the optimization to obtain both mesh-independent designs and to ensure a well-posed optimization formulation [5]. The most common approach is to use filtering [1] enforcing a length scale. Thus, using a finer mesh for the same regularization does not provide additional design freedom and does not allow for smaller design features in the optimized solutions.

Although unstructured meshes as well as filtering for the regularization are applied, the present numerical experiments demonstrate that for almost identical meshes numerical mesh-dependent local minima are frequently obtained even for a filter radius being much larger than the element sizes. Fig. 1a shows an L-shape model being investigated in detail in Section 5. Fig. 1b shows the optimized designs for a compliance topology optimization using two different but very similar meshes. Although all parameters for the optimization formulation, such as the filter size, are the same, then significantly different optimized designs are obtained. This is due to the inaccuracies of the numerical representation of the structural object to be modeled, namely, finite precision finite element meshes and intermediate transition areas present in density-based topology optimization. Subsequently, the optimized design for mesh 2 is shown to be a mesh-induced local minimum. Analyzing the proposed method for suppressing such mesh-induced local minima suggests that mesh-induced local minima are mainly caused by the rough surface discretization of the optimized designs. This applies to all optimization parametrizations using a fixed mesh of the design domain, not being able to apply body-fitted meshes with respect to the surface representation of the optimized design.

Additionally, enforcing a minimal length scale through filtering ensures the manufacturability of optimized designs [6]. However, simple filtering approaches are not always able to enforce a length scale, e.g., compliant mechanism optimization [7]. Unphysical hinges occur at single nodes in the mesh or lumped regions having intermediate density elements occur to mimic a compliant hinge [8]. Therefore, these hinge regions are highly mesh-dependent. A comparison of different filtering techniques is provided in [7]. A review on more advanced approaches, e.g., projection filters, is provided in [6] including robust optimization techniques for the material location with respect to under- and overetching. Similar approaches are also applied to enforce a minimal length scale. Therefore, the present work also investigates the compliant force inverter introduced in [8] and suggested as a reference benchmark in [7], as the compliant force inverter typically has unphysical compliant hinges for deterministic optimization approaches.

Numerical mesh-dependence can be considered as epistemic uncertainty since it is possible to reduce the uncertainty using improved modeling [9], i.e., applying finer meshes. Typically, how fine a mesh is required for achieving mesh-independence is unknown. Commonly, robust design optimization approaches consider aleatoric uncertainties, but might also be able to address uncertainties originating from the numerical mesh discretization and, therefore, are also briefly discussed in the following.

Robust design optimization not only optimizes for deterministic parameters, but also considers some uncertain parameters and some probabilistic measure of the response. Thus, the response surface for the optimization usually yields a smoother surface and thereby reduces the likelihood of ending up in a local minimum [10]. For quantifying the probabilistic measure of the response (e.g., mean and variance), approximation methods are required for the uncertainty propagation. The most straightforward approach is the Monte Carlo method [11]. Although it is generally applicable to non-parametric optimization problems as topology optimization [12], then Monte Carlo methods have extremely high computational costs. Using surrogate models to improve the computational efficiency suffers the curse of dimensionality [13]. Therefore, often local Taylor expansion-based approaches are applied for the uncertainty quantification in the context of robust design optimization [10,14–22]. The drawback is that the gradient of the probabilistic measure with respect to the design variables is less straightforward to evaluate. Doltsinis & Kang [14,15] apply a Taylor expansion of the discretized static equilibrium and the adjoint method to determine mean and variance of the response as well as the corresponding gradients. This approach has been applied to topology optimization by Lazarov et al. [16], showing the advantages over sampling-based methods. Instead of perturbing the static equilibrium, the response function is approximated locally using a Taylor series expansion, which significantly reduces the computational costs. Using a first-order Taylor expansion requires at most three additional solutions of the adjoint equation systems [17]. For second-order approaches the computational cost scales (at least) linearly with the number of random parameters [18,19]. While the aforementioned approaches require highly intrusive numerical implementations, Steltner et al. [10,20] and Krüger et al. [19,21] propose semi-intrusive approaches of Taylor expansion-based robust optimization.

All previously mentioned works on robust optimization consider aleatoric uncertainties of the applied loads, the material properties, or the geometry. To the best of the authors' knowledge, robust optimization methods have not been specifically used to address epistemic uncertainty. Approaches that consider geometric deviations, however, might also be suitable to capture the uncertainty of the mesh discretization. In the literature, different parametrization approaches are presented for geometrical uncertainties. Jansen et al. [23] implement geometrical uncertainties using a randomly perturbed density filter, where the mesh is not affected by the uncertainties. Whereas [18] implements geometrical uncertainties using a direct geometrical perturbation of the nodes of the finite element mesh. Another method describes the geometrical uncertainties assuming a distribution for the projection parameter of the Heaviside projection; see [12]. Uncorrelated geometrical nodal uncertainties are applied in [24]. However, the uncorrelated uncertainties are used to model manufacturing uncertainties for discrete truss structures. Uncertainty formulations for continuum models generally assume a spatial correlation tied to a specific correlation length, enforcing the uncertainty formulation to be independent of the nodes of the finite element model.

Considering mesh perturbation in the same way as geometric uncertainties is considered in the aforementioned references, but does not resolve the problem of obtaining mesh-dependent optimization results. The reason is that applied geometric uncertainties are modeled using random fields, where the spatial correlation smears out local effects. Therefore, the current work suggests to geometrically perturb the nodal coordinates independently, i.e., without considering spatial correlation. Such an approach entails two challenges. Firstly, without spatial correlation for the geometrical uncertainties, the number of random parameters cannot be reduced, e.g. using techniques such as Karhunen-Loève expansion or EOLE method [25]. The present challenge is circumvented using an approach where the computational cost is independent of the number of random parameters. Secondly, without spatial correlation for the uncertainties, the standard deviation of the response is mesh-dependent. Therefore, we propose an L^p-norm-based uncertainty measure instead of the standard deviation. Afterward, we show that for $p = 1$ the present uncertainty measure is independent of the mesh discretization, and when embedded into a robust design optimization formulation then the present uncertainty measure allows for determining mesh-independent minima. Furthermore, we show that for higher values of p, the uncertainty measure enables the suppression of highly localized phenomena like compliant hinges or stress singularities.

The paper is structured as follows. Initially, the theoretical background is summarized. Then, the proposed approach combining uncorrelated nodal uncertainties with an L^p-norm-based uncertainty measure is introduced. In Section 4, we discuss the numerical implementation for the optimization workflow. The numerical result section is divided into one part showing the successful suppression of mesh-dependence for various applications, and the second part containing applications for robustness with respect to highly localized geometrical effects.

2. Theory

2.1. Optimization problem formulation

Non-parametric structural optimization is an iterative process determining the optimized structural properties of a mechanical model. A general optimization formulation reads

$$\begin{cases} \min\limits_{\boldsymbol{\phi}} f_0(\boldsymbol{\phi}) \\ \text{s.t.} \begin{cases} \boldsymbol{R}(\boldsymbol{\phi}, \boldsymbol{u}(\boldsymbol{\phi})) = \boldsymbol{0} \\ f_i(\boldsymbol{\phi}, \boldsymbol{u}(\boldsymbol{\phi})) \leq 0 \\ \boldsymbol{\phi}_L \leq \boldsymbol{\phi} \leq \boldsymbol{\phi}_U \end{cases} \end{cases}, \tag{1}$$

where f_0 is the objective function subject to the finite element residual $\boldsymbol{R}(\boldsymbol{\phi}, \boldsymbol{u}(\boldsymbol{\phi}))$ implicitly defining the response of the system, and f_i is a general set of inequality constraints. The design vector $\boldsymbol{\phi}$ is constrained by the lower and upper bounds $\boldsymbol{\phi}_L$ and $\boldsymbol{\phi}_U$, respectively. For topology optimization, the design variable $\boldsymbol{\phi}$ defines the relative density of each design element and the solid isotropic material interpolation with penalization (SIMP) approach [26] is applied. Thus, $\boldsymbol{\phi}$ is bounded between zero and one. Compliance is frequently chosen as the objective function f_0 to be minimized subject to a relative volume or mass constraint f_i. For the thickness sizing optimization, the design variable is the thickness of each shell element. All numerical examples assume linear finite element modeling. However, this is not a requirement of the proposed method, which can be directly applied to examples using nonlinear finite element modeling. Still, future work needs to verify whether the same conclusions also apply to nonlinear models.

Additionally, a regularization of the design variable is required for the topology optimization problem in (1) to be well-posed. Therefore, filtering introduced in [1] is applied to achieve mesh-independence, introduce a length scale, and prevent checkerboarding. An overview of different filter types and their properties can be found in [7]. In this work, a cone-shaped sensitivity filter [27] as well as a design variable filter based on successive erode and dilate operations [28] are applied. Subsequently, the optimization problem is solved iteratively using a mathematical programming-based Method of Moving Asymptotes proposed in [29].

For robust design optimization, some of the input parameters are assumed to be randomly distributed. Therefore, any response is a random variable given by an unknown probability distribution. Hence, the deterministic response function is replaced by a weighted function of the mean μ_f and the standard deviation σ_f as follows

$$f_r(\boldsymbol{\alpha}, \boldsymbol{\phi}) = \mu_f(\boldsymbol{\alpha}, \boldsymbol{\phi}) + \kappa\sigma_f(\boldsymbol{\alpha}, \boldsymbol{\phi}), \tag{2}$$

where $\boldsymbol{\phi}$ is the vector containing the design variables, $\boldsymbol{\alpha}$ is the vector containing the random variables and κ is a weighting factor defining the impact of the standard deviation. The present robust response function f_r can be applied either as an objective function or as a constraint.

2.2. *Taylor expansion-based robustness approach*

The mean μ_f and standard deviation σ_f with respect to uncorrelated distributions, characterized by the mean $\mu_{\alpha,i}$ and the standard deviation $\sigma_{\alpha,i}$, are approximated using a first-order Taylor expansion as

$$\mu_f \approx f(\boldsymbol{\mu}_\alpha), \quad \text{where} \quad \boldsymbol{\mu}_\alpha = (\mu_{\alpha,1}, \dots, \mu_{\alpha,i}, \dots, \mu_{\alpha,M})^{\mathrm{T}}, \tag{3}$$

$$\sigma^2{}_f \approx \sum_{i=1}^{M} \frac{df(\boldsymbol{\mu}_\alpha)}{d\alpha_i}^2 \sigma^2_{\alpha,i}, \tag{4}$$

where M is the total number of random parameters; see [30] for detailed derivations. Here, all random parameters are assumed to be uncorrelated. This can be achieved using a simple linear transformation and, therefore, causes no loss of generality. Thereby, the corresponding gradients with respect to the design variables $\boldsymbol{\phi}$, required for the optimization, read

$$\frac{d\mu_f}{d\boldsymbol{\phi}} = \frac{df(\boldsymbol{\mu}_\alpha)}{d\boldsymbol{\phi}}, \tag{5}$$

$$\frac{d\sigma^2{}_f}{d\boldsymbol{\phi}} = 2\sum_{i=1}^{M} \frac{d^2 f(\boldsymbol{\mu}_\alpha)}{d\alpha_i d\boldsymbol{\phi}} \frac{df(\boldsymbol{\mu}_\alpha)}{d\alpha_i} \sigma^2_{\alpha,i}. \tag{6}$$

For linear approximations, the mean value is equal to the deterministic response function. The gradient of the standard deviation with respect to the design variable is then calculated using the chain rule as

$$\frac{d\sigma_f}{d\boldsymbol{\phi}} = \frac{1}{2\sigma_f} \frac{d\sigma^2_f}{d\boldsymbol{\phi}}. \tag{7}$$

Calculating the mixed second-order derivatives in (6) can be demanding in terms of computational time and memory. The adjoint method eliminates the computation of the second derivatives, but the adjoint system differs for every combination of the response function and the random variable.

The principal sensitivity First-Order Second-Moment method (ps-FOSM; see [21] for a detailed derivation) reformulates the gradient of the variance so that only one directional derivative is required in addition to the deterministic gradient $df/d\boldsymbol{\phi}$ and the gradient with respect to the random vector $df/d\boldsymbol{\alpha}$. Hence, if the gradient with respect to the random vector $df/d\boldsymbol{\alpha}$ is available in the finite element implementation, then the robust sensitivities can be calculated using only one single non-intrusive finite difference evaluation. For instance, when considering geometrical uncertainty, then the derivative with respect to node positions can be mapped to arbitrary uncertainty parameterizations. The present gradient $df/d\boldsymbol{\alpha}$ is available in the finite element solver Simulia Abaqus [31], where the nodal gradients are traditionally applied for gradient-based shape optimization.

When assuming equal and uncorrelated distributions of the random variables, then the principal sensitivity direction equals

$$\Delta\boldsymbol{\alpha} = \epsilon\sigma^2_\alpha \frac{df}{d\boldsymbol{\alpha}}(\boldsymbol{\mu}_\alpha). \tag{8}$$

Inserting a finite difference step into the direction (8) and reordering yields the gradient of the variance as

$$\frac{d\sigma^2_f}{d\boldsymbol{\phi}} \approx \frac{2}{\epsilon}\left[\frac{df}{d\boldsymbol{\phi}}(\boldsymbol{\mu}_\alpha + \Delta\boldsymbol{\alpha}) - \frac{df}{d\boldsymbol{\phi}}(\boldsymbol{\mu}_\alpha)\right]. \tag{9}$$

Note, ϵ is a scaling factor that must be chosen properly; see [21].

3. Proposed numerical robustness method

The present work aims to achieve robust optimized solutions with respect to the geometrical nodal coordinates of the finite element mesh. A potential approach could be to consider the mesh as a discretized random field, assuming a correlation function, and then solve the robust design optimization problem using (2). Nevertheless, numerical experiments show that such approaches do not solve the optimization problem consistently, as different meshes cause rather different optimized designs. Furthermore, the choice of the correlation function cannot be determined or justified if there is no physical uncertainty to be modeled, i.e., the "correct" correlation function cannot be observed in measurements. This observation motivates the approach presented in this section. Firstly, we define an uncertainty parametrization where the geometrical nodal positions are modeled without any assumptions on the correlation. Secondly, a new uncertainty measure is introduced based on an uncorrelated nodal uncertainty. Finally, the gradient of the present geometrical uncertainty measure is derived, and several aspects of the numerical implementation are discussed.

3.1. *Nodewise geometrical uncorrelated local distributions*

In order to enforce as few assumptions as possible, we consider each coordinate of each node as independent random variable α; see Fig. 2. The mean of each variable equals the nominal value and the standard deviation is denoted σ_α. As shown later, the choice of σ_α is omitted. No specific distribution type is assumed.

The choice of having no correlation between the geometrical nodal positions might appear counterintuitive. If the scatter of the nodal positions was used to model geometric variation as in [18], then the mesh is a discretization of the random field describing

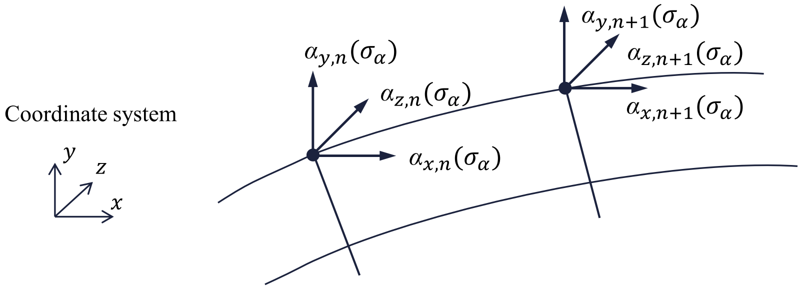

Fig. 2. Nodewise local uncorrelated geometrical distribution α at the discrete coordinates of the nodes i and $i+1$. Each coordinate is considered as independent random variable characterized by the same probability distribution and standard deviation σ_α.

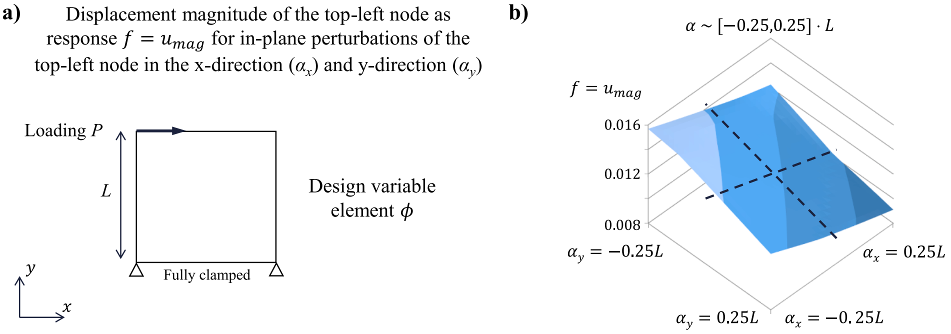

Fig. 3. (a) The variation of the displacement magnitude $f = u_{mag}$ as response of the in-plane geometrical perturbations α_x and α_y in x-direction and y-direction of the top-left node, respectively. (b) The variation of $f = u_{mag}$ for the geometrical perturbations α_x and α_y of a four-node plane stress element (CPS4 [31]). The numerical study shows a linear dependence of the displacement magnitude upon the small nodal geometrical perturbations.

the geometrical uncertainty. Hence, some spatial correlation is to be expected. However, we are modeling epistemic uncertainty, and any spatial correlation smears out local effects, which avoids obtaining the desired numerical robustness against geometrical mesh distributions.

Not choosing a spatial correlation comes with two drawbacks. Firstly, using a correlation allows to reduce the number of random variables for example using the Karhunen–Loève expansion or the EOLE method [25]. Usually, the computational cost of most robust optimization approaches scales with the number of random variables causing practically infeasible computational costs for most approaches. However, using a first-order approximation, particularly the ps-FOSM method, imposes that the computational cost is independent of the number of random variables. The validity of using linear approximations for the proposed geometrical uncertainty is shown in Fig. 3. The results in Fig. 3 study the displacement magnitude of a single element as a function of the geometrical variation in the x- and y-coordinates of the loaded node.

The second drawback is that, when modifying or refining the mesh, the shape of the local geometrical perturbations changes, which would be regularized when using a spatial correlation function. Although this is intended by the proposed approach, then modeling or refining the mesh causes changes in the standard deviation of the response function as the number and location of the nodes of the mesh change. Therefore, in the following, a new uncertainty measure different from the standard deviation is considered and discussed in the following subsection.

3.2. Novel uncertainty measure for geometrical uncorrelated distributions

This section proposes a novel generalized first-order uncertainty measure using the proposed uncertainty parametrization introduced in Section 3.1.

The standard deviation is commonly selected as an uncertainty measure for scatter [10,12,14–24] due to its mathematical properties. However, using uncorrelated nodal uncertainties as introduced in the Section 3.1 then the standard deviation of a response function depends upon the discretization, i.e., the mesh refinement. Therefore, we suggest an alternative measure for the geometrical scatter.

Kanno [32] reviews different concepts for robust design optimization and shows that different robustness measures can be considered as variants of the L^p-norm-based uncertainty

$$\tilde{\sigma}_f = \left(\sum_{i=1}^{M} \left| \frac{df}{d\alpha_i} \delta_{\alpha_i} \right|^p \right)^{\frac{1}{p}}, \tag{10}$$

where the amount α scatters, is indicated by the scalar δ_α. Considering that f is a linear function of all α_i and assuming the factors α_i to be bounded in intervals of width $2\delta_{\alpha_i}$, then the L^1-norm provides the worst-case combination of α_i. When assuming that all α_i are bounded in a hyper-ellipsoid with semi-axes length $\sqrt{\delta_{\alpha_i}}$, then the L^2-norm provides the worst-case combination of α_i. If δ_{α_i} is the standard deviation of α_i and all α_i are assumed to be uncorrelated, then the L^2-norm equals the standard deviation of the response. Kanno [32] also mentions works in which the L^∞-norm is used as objective, which is approximated using a high exponent p in (10).

For the robustness optimization with respect to discretization uncertainty, we propose using the L^2-norm of the three spatial directions per node and then the L^p-norm to combine the contributions of all nodes. It is necessary to apply the L^2-norm at the nodal level since otherwise isotropy of the proposed measure (i.e., the measure being independent of the chosen coordinate system) is not fulfilled.

In particular, we propose computing the L^2 norm for the uncertainty of a single node given by

$$\sigma_{f,n} = \left(\frac{d f_\mu}{d\alpha_{x,n}}^2 + \frac{d f_\mu}{d\alpha_{y,n}}^2 + \frac{d f_\mu}{d\alpha_{z,n}}^2 \right)^{\frac{1}{2}} \sigma_\alpha . \tag{11}$$

This measure corresponds to the standard deviation of the response f induced by the uncertainty of a single node n and approximated by the FOSM method. Here, σ_α is the standard deviation of the nodal position, which is assumed to be identical in all directions for all nodes, i.e., $\sigma_{\alpha,i} = \sigma_\alpha$. Afterward, we suggest to aggregate the measure in (11) over all geometrical discrete points using the L^p norm, defined as

$$\tilde{\sigma}_f = ||\boldsymbol{\sigma}_f||_p = \left(\sum_{n=1}^{N} \sigma_{f,n}^p \right)^{\frac{1}{p}} = \left(\sum_{n=1}^{N} \left(\sqrt{\left(\frac{d f_\mu}{d\alpha_{x,n}}^2 + \frac{d f_\mu}{d\alpha_{y,n}}^2 + \frac{d f_\mu}{d\alpha_{z,n}}^2 \right)} \sigma_\alpha \right)^p \right)^{\frac{1}{p}} = \left(\sum_{n=1}^{N} \left(\left|\left| \frac{d f_\mu}{d\hat{\boldsymbol{\alpha}}_n} \right|\right|_2 \right)^p \right)^{\frac{1}{p}} \sigma_\alpha . \tag{12}$$

For $p = 1$ and assuming f is linear approximated, the uncertainty measure $\tilde{\sigma}_f$ can be seen as a measure of the worst-case combination of single-node perturbations impacting the response f. For $p = 2$, $\tilde{\sigma}_f$ equals the standard deviation, while for large values of p, $\tilde{\sigma}_f$ approaches the maximum norm and only describes the largest nodal standard deviation present in the structure equal to the most critical location in the structure with respect to a geometrical variation. In the following, the proposed generalized uncertainty measure $\tilde{\sigma}_f$ in (12) is further examined, proving its superiority in comparison to the standard deviation for the proposed geometrical uncertainty parametrization.

For large values of p, a mesh-dependent localized uncertainty measure approximating the largest nodal standard deviation is obtained whereas mesh-independence is recovered for the proposed uncertainty measure using $p = 1$. Since the responses applied in a topology optimization formulation are generally mesh-independent and not affected by rigid body movements of the domain then the integral of $d f_\mu / d\hat{\boldsymbol{\alpha}}_n$ over the domain is equal to zero. Integration over the domain is equivalent to a summation of the nodal values. Consequently, the summation of the magnitudes of $d f_\mu / d\hat{\boldsymbol{\alpha}}_n$ yields a mesh-independent constant.

Fig. 4 shows $d f_\mu / d\hat{\boldsymbol{\alpha}}$ for two different meshes and the compliance response values, as well as the proposed uncertainty measure for $p = 1$ and $p = 2$. Thus, mesh-independence of the proposed uncertainty measure is shown for $p = 1$ as the deterministic response function μ_f changes by $4.1\,\%$ between the two different meshes and the uncertainty measure changes by $3.6\,\%$, which can be considered numerically the same.

Only the fixed standard deviation σ_α must be chosen for the uncertainty measure in (12) when assuming uncorrelated parameters. For the present robust design optimization formulation, the new uncertainty measure $\tilde{\sigma}_f$ in (12) will replace the standard deviation in the objective function given by (2). In addition, the weighting factor κ must be chosen. As shown in (12), σ_α is a linear factor of $\tilde{\sigma}_f$, which is then multiplied by κ. Hence, choosing σ_α and κ is equivalent. Therefore, we set $\sigma_\alpha = 1$ without loss of generality and leave κ as the only parameter to be chosen. Numerical studies show that for $p = 1$ the recommended choice of κ is $\kappa \approx 0.1 \cdot \mu_f / \tilde{\sigma}_f$ of the initial optimization iteration. For other values of p, no general recommendation is provided in the present study, as this is frequently highly model-dependent.

Additionally, Fig. 4 shows that the nodal gradient generally matches the direction of the density gradient for all nodes that are not associated with the boundary conditions or the loading. This is expected since the position of interior nodes should not influence the structural response for a sufficiently fine mesh. However, adding or removing material on the surface has an influence on the value of the structural response. In combination with the mesh-independence of the proposed uncertainty measure for $p = 1$, one concludes that the proposed uncertainty measure is a measure indicating how sensitive the response function is to adding or removing material at the surface. Furthermore, recognizing that the uncertainty is generally tied to a volume change and that the perturbation of a single node inside a checkerboard pattern is volume-preserving, then we conclude that the proposed method cannot impose a minimal length scale. Thus, the proposed method has to be applied in combination with a regularization as discussed in Section 2. Additionally, Sections 5.4 and 6 also discuss the influence of the present robustness approach on the minimal length scale.

3.3. Semi-intrusive gradients with respect to the design variable

The gradient of the uncertainty measure $\tilde{\sigma}_f$ in (12) with respect to the design variable $\boldsymbol{\phi}$ is derived as

$$\frac{d\tilde{\sigma}_f}{d\boldsymbol{\phi}} = \frac{1}{\tilde{\sigma}_f^{p-1}} \sum_{n=1}^{N} \left(\frac{d f_\mu}{d\alpha_{x,n}}^2 + \frac{d f_\mu}{d\alpha_{y,n}}^2 + \frac{d f_\mu}{d\alpha_{z,n}}^2 \right)^{\frac{p}{2}-1} \left(\frac{d f_\mu}{d\alpha_{x,n}} \frac{d^2 f_\mu}{d\boldsymbol{\phi}\, d\alpha_{x,n}} + \frac{d f_\mu}{d\alpha_{y,n}} \frac{d^2 f_\mu}{d\boldsymbol{\phi}\, d\alpha_{y,n}} + \frac{d f_\mu}{d\alpha_{z,n}} \frac{d^2 f_\mu}{d\boldsymbol{\phi}\, d\alpha_{z,n}} \right). \tag{13}$$

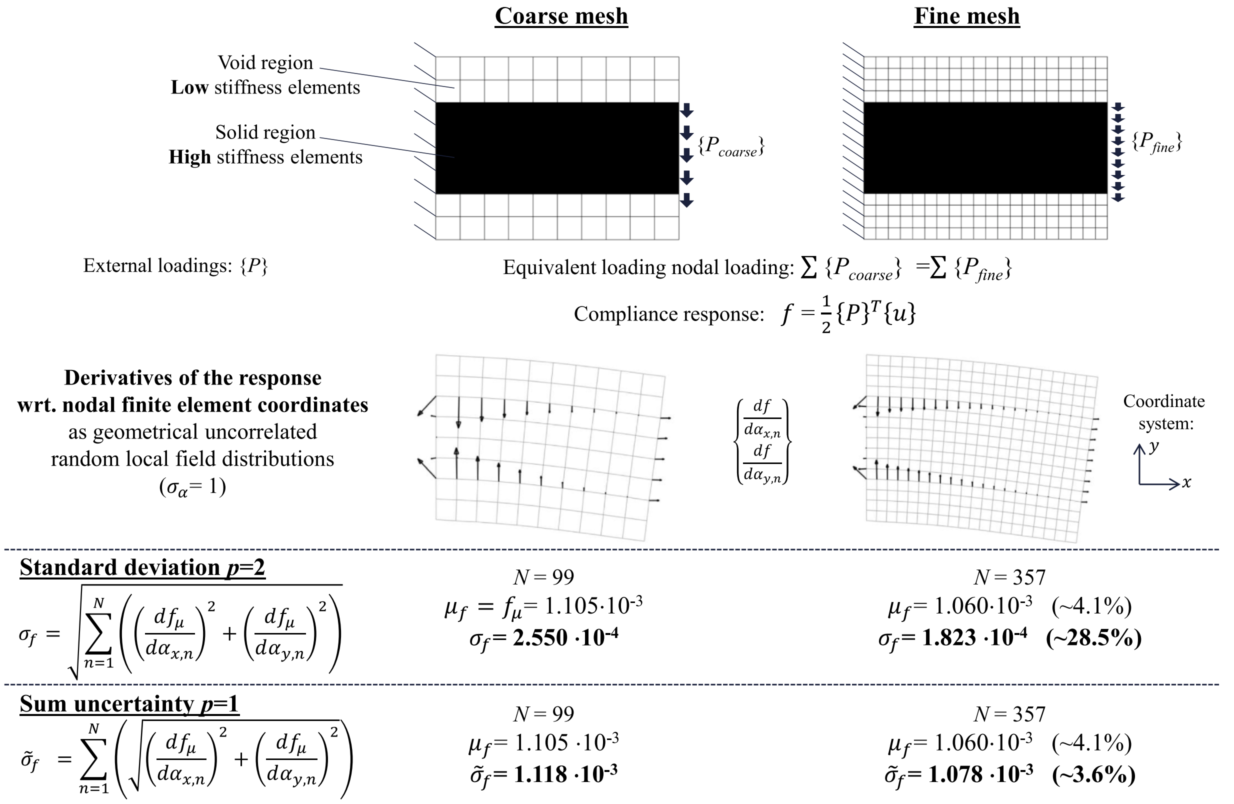

Fig. 4. A mesh sensitivity study using a coarse mesh and a fine mesh where both models are attached equivalently to the same boundary conditions and loading. Both the solid region and void regions of the models are modeled using a linear elastic isotropic material with a Poisson's ratio of 0.3 whereas the solid region has a Young's modulus of 1.0 and the void region has a Young's modulus of $1.0 \cdot 10^{-9}$. The coarse model is meshed by 80 four-node plane stress elements (CPS4 [31]) using 99 nodes, and the fine model is meshed by 320 four-node plane stress elements (CPS4 [31]) using 357 nodes, respectively. The geometrical standard deviation is calculated per node using the derivatives of the response function with respect to the nodal finite element coordinates using FOSM. Subsequently, the compliance response as well as the uncertainty measure (12) for $p = 1$ and $p = 2$ are calculated, respectively.

Note, σ_α is set to one. The principal sensitivity calculation is rather similar to the derivation in [21] based upon a finite difference approximation and is generalized using a first-order Taylor expansion as

$$\frac{df}{d\boldsymbol{\phi}}(\boldsymbol{\mu}_\alpha + \epsilon\Delta\boldsymbol{\alpha}) \approx \frac{df}{d\boldsymbol{\phi}}(\boldsymbol{\mu}_\alpha) + \frac{d^2 f}{d\boldsymbol{\phi}\, d\boldsymbol{\alpha}}(\boldsymbol{\mu}_\alpha)\epsilon\Delta\boldsymbol{\alpha}. \tag{14}$$

Rearranging (14) to be solved using finite differences yields

$$\frac{d^2 f}{d\boldsymbol{\phi}\, d\boldsymbol{\alpha}}(\boldsymbol{\mu}_\alpha)\Delta\boldsymbol{\alpha} \approx \frac{1}{\epsilon}\left[\frac{df}{d\boldsymbol{\phi}}(\boldsymbol{\mu}_\alpha + \epsilon\Delta\boldsymbol{\alpha}) - \frac{df}{d\boldsymbol{\phi}}(\boldsymbol{\mu}_\alpha)\right], \tag{15}$$

where ϵ is a scaling factor. Rewriting (13) to be computed using the general principal sensitivity workflow, similar to [21], yields

$$\begin{aligned}
\frac{d\tilde{\sigma}_f}{d\boldsymbol{\phi}} &= \sum_{n=1}^{N}\left(\frac{d^2 f_\mu}{d\boldsymbol{\phi}\, d\alpha_{x,n}}, \frac{d^2 f_\mu}{d\boldsymbol{\phi}\, d\alpha_{y,n}}, \frac{d^2 f_\mu}{d\boldsymbol{\phi}\, d\alpha_{z,n}}\right)\frac{1}{\tilde{\sigma}_f^{p-1}}\left(\frac{df_\mu}{d\alpha_{x,n}}^2 + \frac{df_\mu}{d\alpha_{y,n}}^2 + \frac{df_\mu}{d\alpha_{z,n}}^2\right)^{\frac{p}{2}-1}\left(\frac{df_\mu}{d\alpha_{x,n}}, \frac{df_\mu}{d\alpha_{y,n}}, \frac{df_\mu}{d\alpha_{z,n}}\right)^{\mathrm{T}} \\
&= \sum_{n=1}^{N}\frac{d^2 f_\mu}{d\boldsymbol{\phi}\, d\hat{\boldsymbol{\alpha}}_n}(\boldsymbol{\mu}_\alpha)\Delta\hat{\boldsymbol{\alpha}}_n = \frac{d^2 f_\mu}{d\boldsymbol{\phi}\, d\boldsymbol{\alpha}}(\boldsymbol{\mu}_\alpha)\Delta\boldsymbol{\alpha} \approx \frac{1}{\epsilon}\left[\frac{df}{d\boldsymbol{\phi}}(\boldsymbol{\mu}_\alpha + \epsilon\Delta\boldsymbol{\alpha}) - \frac{df}{d\boldsymbol{\phi}}(\boldsymbol{\mu}_\alpha)\right], \\
&\quad \text{where} \quad \boldsymbol{\alpha} = \left(\hat{\boldsymbol{\alpha}}_1^{\mathrm{T}}, \dots, \hat{\boldsymbol{\alpha}}_N^{\mathrm{T}}\right)^{\mathrm{T}} \quad \text{and} \quad \hat{\boldsymbol{\alpha}}_n = \left(\alpha_{x,n}, \alpha_{y,n}, \alpha_{z,n}\right)^{\mathrm{T}} \\
&\quad \text{and} \quad \Delta\hat{\boldsymbol{\alpha}}_n = \frac{1}{\tilde{\sigma}_f^{p-1}}\left(\frac{df_\mu}{d\alpha_{x,n}}^2 + \frac{df_\mu}{d\alpha_{y,n}}^2 + \frac{df_\mu}{d\alpha_{z,n}}^2\right)^{\frac{p}{2}-1}\left(\frac{df_\mu}{d\alpha_{x,n}}, \frac{df_\mu}{d\alpha_{y,n}}, \frac{df_\mu}{d\alpha_{z,n}}\right)^{\mathrm{T}}.
\end{aligned} \tag{16}$$

The scaling parameter ϵ is chosen using a generalized finite difference step size as

$$\hat{\epsilon} = \epsilon \max_i(|\Delta\alpha_i|), \tag{17}$$

to be applicable for different choices of p. In the present work, the finite difference step size $\hat{\epsilon}$ is generally chosen to be two orders of magnitude smaller than the characteristic element length. Generally, $\hat{\epsilon}$ has to be significantly smaller than the shortest element edge.

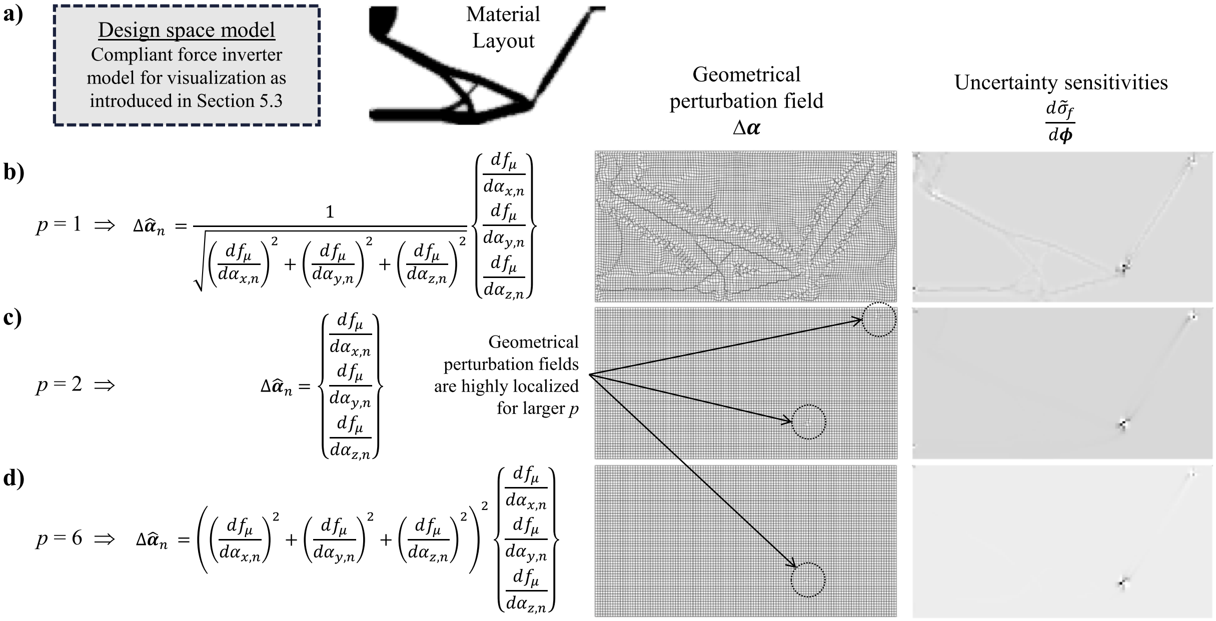

Fig. 5. The geometrical perturbation field $\Delta\boldsymbol{\alpha}$ and the sensitivities $d\tilde{\sigma}_f/d\boldsymbol{\phi}$ given in (16) of the geometrical uncertainty measure with respect to an elemental topology design variable field are visualized for the optimized structure on (a) the design space of the inverter mechanism topology optimization example studied in Sections 5.3 and 6.1 for three different exponents (b) $p = 1$, (c) $p = 2$, and (d) $p = 6$, respectively.

Fig. 5 shows the applied finite difference perturbation using different values of the aggregation parameter p. For values of $p > 1$, this yields highly localized geometrical perturbation fields. The corresponding effects are discussed in Section 6. In contrast, when using $p = 1$, the geometrical perturbations are applied to every node having the same magnitude. The proposed measure using $p = 1$ suppresses mesh-induced local minima as discussed in Section 5. Recalling that $p = 1$ yields a worst-case approximation then one concludes that numerical mesh-dependence might not be dominated by the most sensitive locations of the mesh but by the overall surface discretization of the optimized design.

Generally, the proposed L^p-norm-based uncertainty measure can have numerical challenges for $p = 1$ as well as $p >> 1$. Thus, additional implementation details are provided in Appendix A. Specifically, for $p = 1$ the denominator of the principal sensitivity perturbation might approximate zero yielding numerical overflows as visualized in Fig. 5. Thus, a threshold scheme is proposed in Appendix A.1. For large values of p, numerical overflows are prevented using a normalization as derived in Appendix A.2. Additionally, numerical regularization using filtering of the nodal gradients is proposed in Appendix A.3 and improves the convergence for the localized uncertainty measure using large values of p as demonstrated in Section 6.

To practically model geometrical mesh uncertainty for shell element models the uncertainty parametrization should be strictly in-plane as discussed in Appendix B.1. Additionally, the response with respect to the uncertainty parametrization for shell elements will not be fully linear. Thus, central finite differences are applied instead of forward finite differences for the sensitivity calculation; see Appendix B.2.

4. Numerical implementation

Fig. 6 shows a common deterministic optimization workflow that is extended to also include geometrical robustness in the optimization formulation using a semi-intrusive implementation. Note, an additional adjoint system is solved for the nodal gradients of the deterministic design, and subsequently, an additional finite element analysis is required for the geometrical perturbed mesh to determine the robust response as well as the corresponding gradients with respect to the design variable.

The proposed numerical robustness method is implemented using the software solutions from Dassault Systèmes. Specifically, the optimization tool Tosca Structure [33] in combination with the structural solver Abaqus [31] is applied. Additional calculations and interface modifications are handled using Python scripts.

Abaqus provides the nodal derivatives of the response with respect to the coordinate directions, which are for the present approach by definition the derivatives with respect to the geometrical random variables. The finite difference evaluations are performed using additional Abaqus finite element analyses for the perturbed meshes. The robust response function f_r and the corresponding sensitivities with respect to design variables are then parsed into Tosca Structure where a Method of Moving Asymptotes [29] modifies the design variables in each optimization iteration.

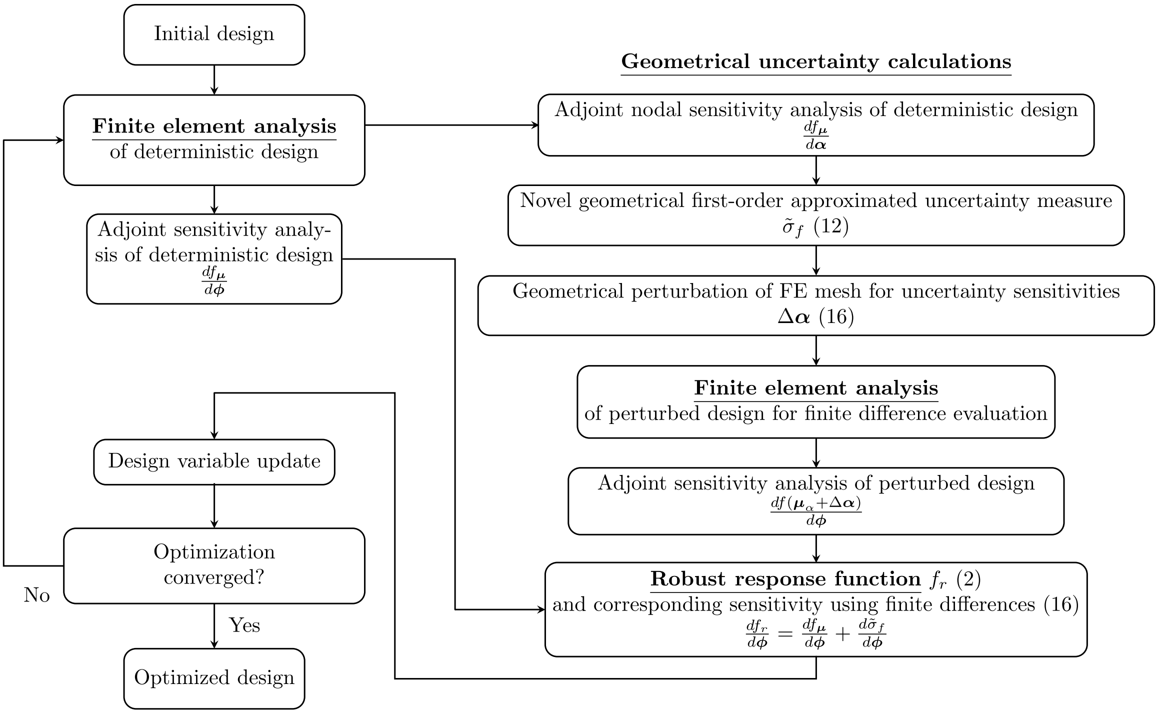

Fig. 6. Deterministic optimization workflow extended for robustness with respect to nodal geometrical uncertainty.

5. Numerical results for mesh robustness

Setting $p = 2$ is the same as calculating the standard deviation using the original FOSM method, as discussed in Section 3.2. Therefore, the proposed method is initially applied to the L-shape example using $p = 2$ for completeness. Conversely, choosing $p = 1$ and $p > 2$ shows the full potential of the proposed method and the present uncertainty parametrization. Setting $p = 1$ significantly improves numerical robustness regarding numerical mesh uncertainty. On the other hand, as shown in Section 6, large values of p enhance the manufacturability of compliant hinges and show compliance optimized designs being comparable to stress-constrained optimized designs.

Initially, two examples showing numerical mesh-dependence having two very similar meshes are investigated. Specifically, the L-shape in Section 5.1 modeled using shell elements and the crane hook in Section 5.2 as a 3D continuum model. Secondly, the compliant force inverter example in Section 5.3 is analyzed to demonstrate mesh sensitivity across different mesh types and element sizes. Lastly, an aircraft bracket is investigated in Section 5.4. This last case study offers insights into distinguishing between numerical and physical local minima.

5.1. L-Shape

The L-shape example is clamped at the two holes and loaded at the top through a pressure load as shown in Fig. 7. The compliance is minimized subject to a relative mass constraint of 50 %. Two different meshes having only minor differences as shown in Fig. 7c and d are applied for the optimizations. The two meshes consist of slightly different numbers of three- and four-node shell elements (S3 and S4 [31]).

Figs. 8a, b, 9 and 10a, b show the deterministic topology-optimized designs using the two meshes and apply a sensitivity and a density filter, respectively. The deterministic optimized designs in Figs. 8a, b and 9 for the sensitivity filter are mesh-dependent and at least the optimized solution for mesh 2 is a local minimum, since the compliance is significantly larger than the compliance of the optimized design for mesh 1. The deterministic optimized designs in Fig. 10a and b are mesh-independent. However, the appearance of the two arms and the optimized compliance values in contrast to the optimized solution using mesh 1 in Fig. 8a suggests the optimized designs attain the same local minimum. Fig. 11a and b shows the deterministic thickness sizing optimized designs using the two different meshes. The optimized designs seem mesh-independent. However, the optimized designs consist of two arms similar to the local minimum obtained using topology optimization.

Fig. 8 shows the deterministic and the robust optimized designs of the L-shape. First, the standard deviation ($p = 2$) is applied for the robust optimization. Note, the filter radius for the sensitivity filter is the same for all six optimized designs. The two robust optimized designs for $\kappa = 0.1$ in Fig. 8e and f have similar optimized designs, which is expected as the differences in the two finite

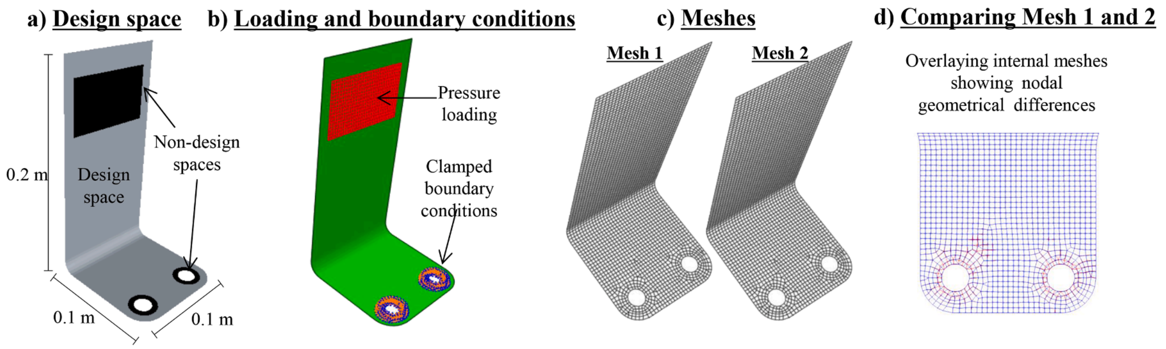

Fig. 7. (a) Design space of an L-bracket applied for a topology and a sizing optimization, respectively. The material is modeled as linear elastic isotropic material with a Poisson's ratio of 0.3 and a Young's modulus of 147 GPa, and the filter radius is set to 3.88 mm. (b) The compliance for the given pressure load of 100 Pa and boundary conditions is minimized as objective function subject to a relative mass constraint of 50 %. (c) The model is first meshed with 13 S3 three-node and 3275 S4 four-node 3D shell elements having 3426 nodes and secondly, the model is meshed by 19 S3 three-node and 3265 S4 four-node 3D shell elements having 3418 nodes. (d) A mesh comparison shows that the two meshes are generally rather similar.

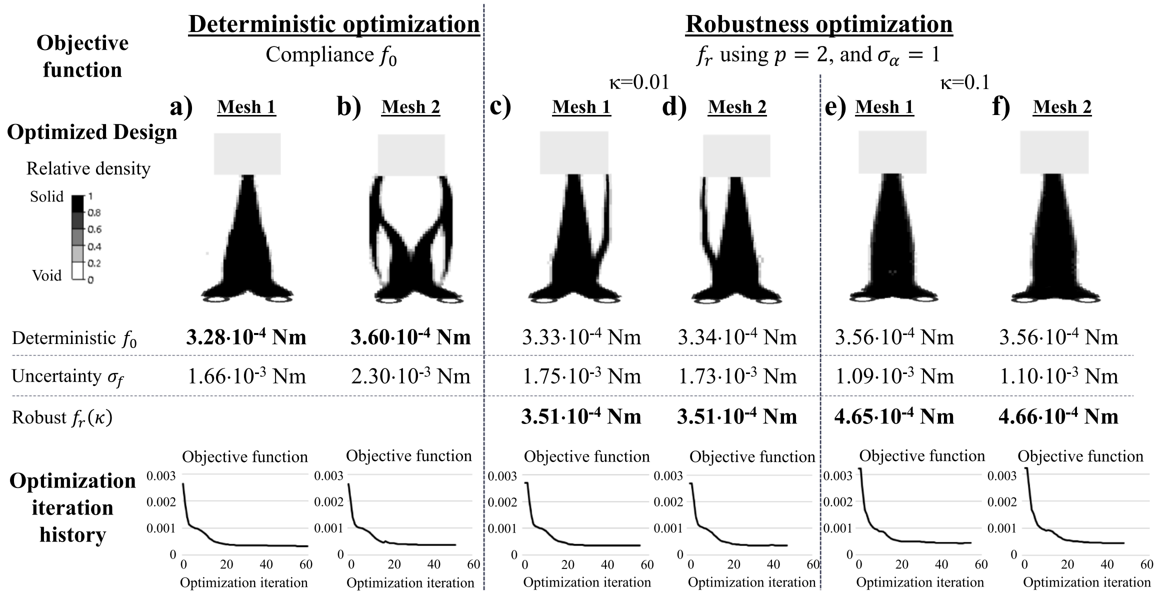

	a) Mesh 1	b) Mesh 2	c) Mesh 1	d) Mesh 2	e) Mesh 1	f) Mesh 2
Deterministic f_0	**$3.28\cdot10^{-4}$ Nm**	**$3.60\cdot10^{-4}$ Nm**	$3.33\cdot10^{-4}$ Nm	$3.34\cdot10^{-4}$ Nm	$3.56\cdot10^{-4}$ Nm	$3.56\cdot10^{-4}$ Nm
Uncertainty σ_f	$1.66\cdot10^{-3}$ Nm	$2.30\cdot10^{-3}$ Nm	$1.75\cdot10^{-3}$ Nm	$1.73\cdot10^{-3}$ Nm	$1.09\cdot10^{-3}$ Nm	$1.10\cdot10^{-3}$ Nm
Robust $f_r(\kappa)$			**$3.51\cdot10^{-4}$ Nm**	**$3.51\cdot10^{-4}$ Nm**	**$4.65\cdot10^{-4}$ Nm**	**$4.66\cdot10^{-4}$ Nm**

Fig. 8. Topology optimization results using the sensitivity filter for the two models defined in Fig. 7. The sensitivity filter radius is the same for all six optimized designs. The deterministic optimization results for (a) mesh 1 and (b) mesh 2 and the robust optimization results for (c,e) mesh 1 and (d, f) mesh 2 applying the standard deviation ($p = 2$) for $\sigma_\alpha = 1$, and (c, d) $\kappa = 0.01$ and (d, f) $\kappa = 0.1$ for the objective function to be minimized. The deterministic designs (a) and (b) have f_0 as the objective function to be minimized whereas the robust designs (c), (d), (e), and (f) have f_r as the objective function to be minimized. Additionally, the optimization iteration histories of the objective function for all six designs are shown.

element meshes are very minor. Thereby, the robust topology optimization results using $\kappa = 0.1$ are numerical mesh-independent when the standard deviation is included as numerical robustness in the optimization formulation.

The two robust optimized designs for $\kappa = 0.01$ in Fig. 8c and d have numerically identical optimized response functions, while the optimized designs are mirrored about the center line. The robust optimized designs in Fig. 8c and d also have lower deterministic compliance f_0 than the deterministic optimized design in Fig. 8b even though the robust optimized designs are optimized for the robust compliance f_r. However, the design shown in Fig. 8a remains the design with the lowest deterministic compliance f_0.

The robust optimized designs in Fig. 8e and f have numerically the same deterministic response function as the deterministic optimized design in Fig. 8b. However, the optimized density distribution is more similar to the deterministic optimized design in Fig. 8a.

In conclusion, the proposed nodewise uncorrelated uncertainty parametrization using the FOSM method suppresses the likelihood of ending up in a mesh-induced local minimum. However, the method also causes side effects that are investigated and characterized in Section 6 using larger values for the aggregation parameter p. Thus, the robust optimized designs do not have the optimal deterministic

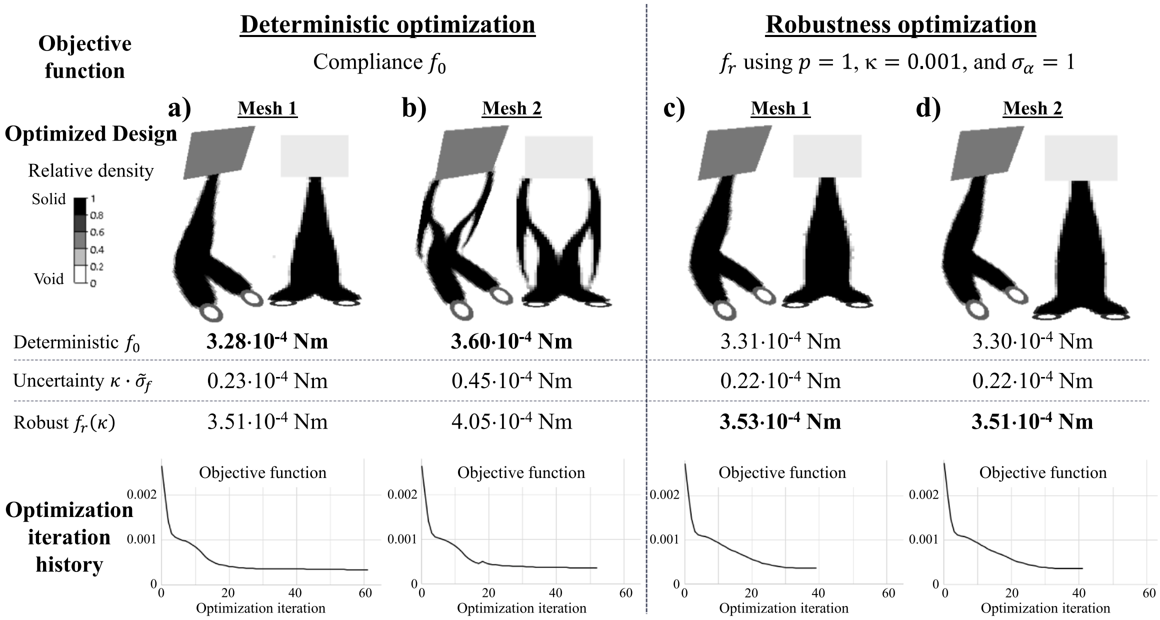

Fig. 9. Topology optimization results using the sensitivity filter for the two models defined in Fig. 7. The sensitivity variable filter radius is the same for all four optimized designs. The deterministic optimization results for (a) mesh 1 and (b) mesh 2 and the robust optimization results for (c) mesh 1 and (d) mesh 2 applying the novel sum uncertainty ($p = 1$) for $\sigma_\alpha = 1$ and $\kappa = 0.001$ for the objective function to be minimized. Thus, the designs (a) and (b) have f_0 as the objective function compliance to be minimized whereas the designs (c) and (d) have f_r as the objective function compliance to be minimized. Additionally, the optimization iteration histories of the objective function for all four designs are shown.

response function value. The desired mesh-independence, isolated from the described side effects, is obtained using $p = 1$ and is hence applied in the following studies.

The proposed uncertainty measure using $p = 1$ is a sum of nodal standard deviations, where each standard deviation has the same weight and, as introduced in Section 3.2, satisfies mesh-independence.

Figs. 9 and 10 show the topology-optimized designs and Fig. 11 shows the thickness sizing optimized designs where the thickness of each shell element is a design variable. A sensitivity filter is applied for the topology optimization shown in Fig. 9 and for the thickness sizing optimization shown in Fig. 11 whereas a design variable filter is applied for the topology optimization in Fig. 10. Note, the filter radius for the design variable filter and for the sensitivity filter is the same for all 12 optimized designs shown in Figs. 9–11.

The topology optimization results shown in Fig. 9 using the sensitivity filter show that, in contrast to the two deterministic optimized designs, the two robust optimized designs in Fig. 9 have numerically identical optimized designs. Thus, the robust topology optimization results are numerical mesh-independent when the novel sum uncertainty for $p = 1$ is included as numerical robustness in the optimization formulation. Additionally, the robust optimization using the sensitivity filter requires fewer optimization iterations than the corresponding deterministic optimization.

The topology optimization results shown in Fig. 10 using the design variable filter show that the two deterministic optimized designs and the two robust optimized designs are similar, but the robust optimized designs have a better structural performance.

The thickness sizing optimization results shown in Fig. 11 yield the same conclusions as the topology optimization using the design variable filter in Fig. 10.

The robust optimized designs shown in Figs. 9c, d, 10c, d, 11c, and d also have lower deterministic compliance f_0 than the corresponding deterministic optimized designs shown in Figs. 9b, 10a, b, 11a, and b even though the robust optimized designs are optimized for robust compliance f_r. Thus, the novel sum uncertainty using $p = 1$ in the robust optimization formulation for the present applications suppresses the likelihood of ending up in a local minimum.

The numerical optimization results show that the same conclusions are reached for topology optimization and thickness sizing optimization, showing that the present robust optimization formulation using the novel sum uncertainty for $p = 1$ is independent of the design variable type for non-parametric optimization (e.g., other design variables types could be nodal shape design variables, bead design variables, composite layered thickness, composite layered angles, etc.). Secondly, we observe that the robust optimization requires a similar number of optimization iterations as the deterministic optimization.

5.2. Crane hook

The crane hook model is clamped at the top hole and loaded through distributed forces using two load cases as shown in Fig. 12. The compliance is minimized subject to a volume constraint of 50 %.

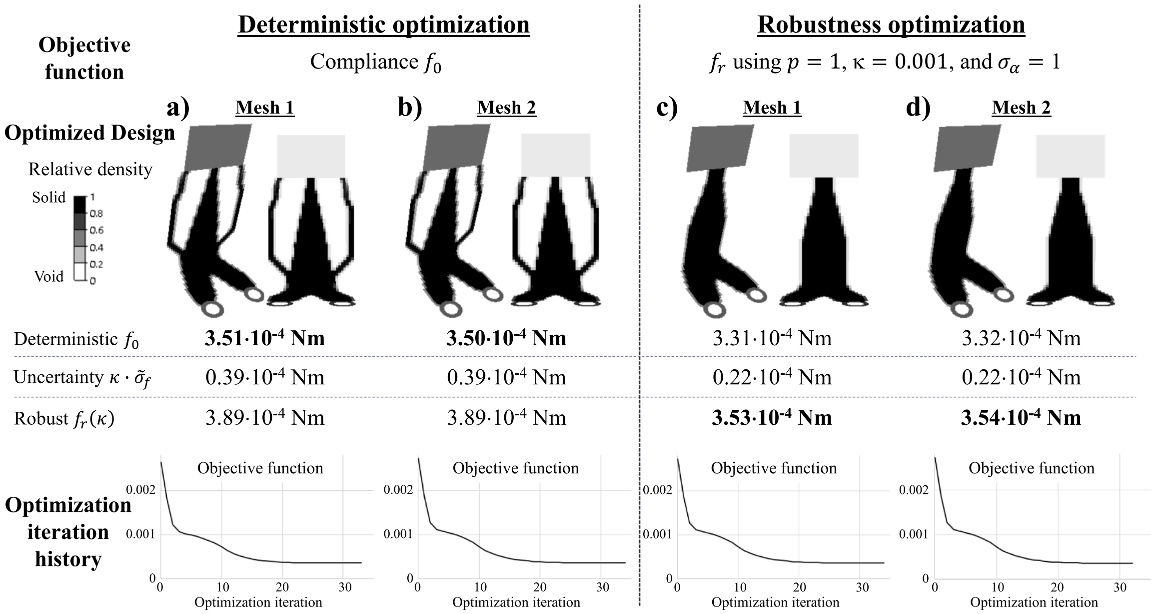

	a) Mesh 1	b) Mesh 2	c) Mesh 1	d) Mesh 2
Deterministic f_0	**3.51·10^{-4} Nm**	**3.50·10^{-4} Nm**	3.31·10^{-4} Nm	3.32·10^{-4} Nm
Uncertainty $\kappa \cdot \tilde{\sigma}_f$	0.39·10^{-4} Nm	0.39·10^{-4} Nm	0.22·10^{-4} Nm	0.22·10^{-4} Nm
Robust $f_r(\kappa)$	3.89·10^{-4} Nm	3.89·10^{-4} Nm	**3.53·10^{-4} Nm**	**3.54·10^{-4} Nm**

Fig. 10. Topology optimization results using the design variable filter for the two models defined in Fig. 7. The design variable filter radius is the same for all four optimized designs. The deterministic optimization results for (a) mesh 1 and (b) mesh 2 and the robust optimization results for (c) mesh 1 and (d) mesh 2 applying the novel sum uncertainty ($p = 1$) for $\sigma_\alpha = 1$ and $\kappa = 0.001$ for the objective function to be minimized. Thus, the designs (a) and (b) have f_0 as the objective function compliance to be minimized, whereas the designs (c) and (d) have f_r as the objective function compliance to be minimized. Additionally, the optimization iteration histories of the objective function for all four designs are shown.

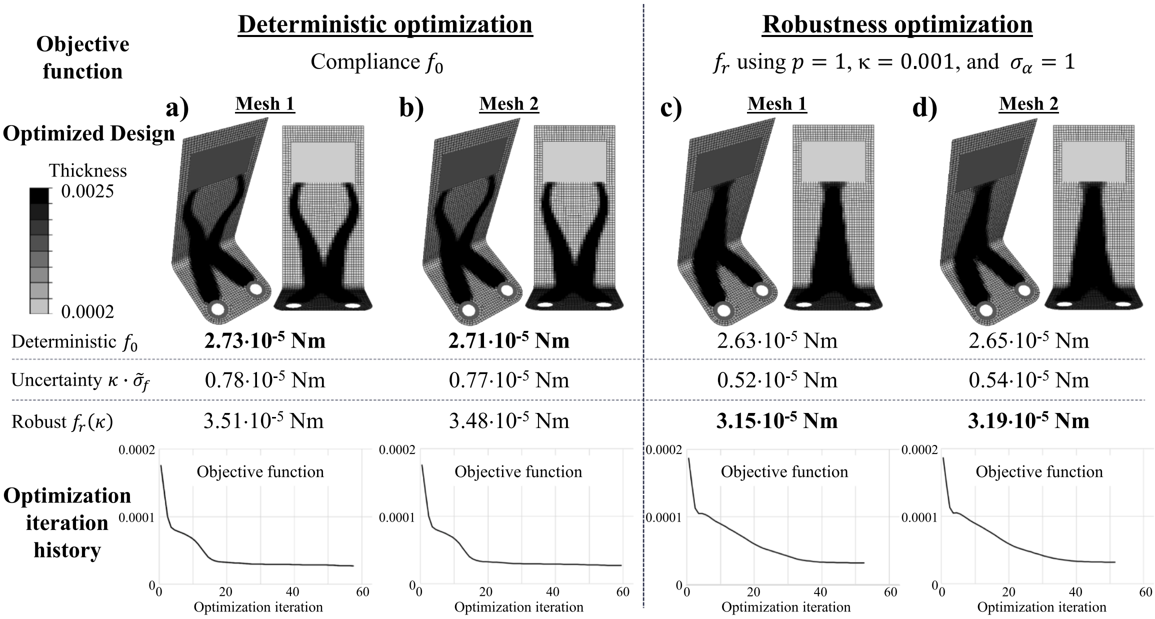

	a) Mesh 1	b) Mesh 2	c) Mesh 1	d) Mesh 2
Deterministic f_0	**2.73·10^{-5} Nm**	**2.71·10^{-5} Nm**	2.63·10^{-5} Nm	2.65·10^{-5} Nm
Uncertainty $\kappa \cdot \tilde{\sigma}_f$	0.78·10^{-5} Nm	0.77·10^{-5} Nm	0.52·10^{-5} Nm	0.54·10^{-5} Nm
Robust $f_r(\kappa)$	3.51·10^{-5} Nm	3.48·10^{-5} Nm	**3.15·10^{-5} Nm**	**3.19·10^{-5} Nm**

Fig. 11. Thickness sizing optimization results using the sensitivity filter for the two models defined in Fig. 7. The sensitivity variable filter radius is the same for all four optimized designs. The deterministic optimization results for (a) mesh 1 and (b) mesh 2 and the robust optimization results for (c) mesh 1 and (d) mesh 2 applying the novel sum uncertainty ($p = 1$) for $\sigma_\alpha = 1$ and $\kappa = 0.001$ for the objective function to be minimized. Thus, the designs (a) and (b) have f_0 as the objective function compliance to be minimized whereas the designs (c) and (d) have f_r as the objective function compliance to be minimized. Additionally, the optimization iteration histories of the objective function for all designs are shown.

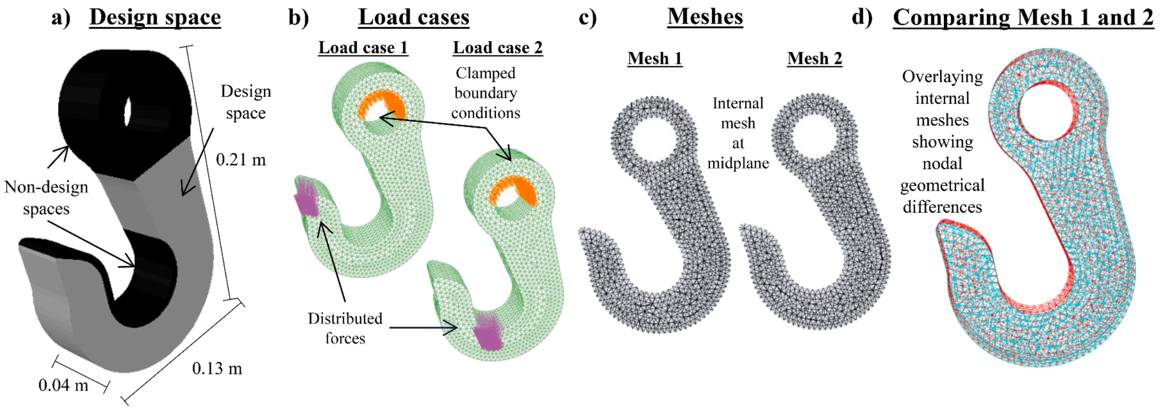

Fig. 12. (a) Design space for a crane hook topology optimization. The material is modeled as linear elastic isotropic material with a Poisson's ratio of 0.3 and a Young's modulus of 210 GPa, and the filter radius is set to 9.73 mm. (b) The total compliance for two load cases (being distributed forces of 15.43 N/mm^2 and 11.23 N/mm^2, respectively) is minimized as objective function subject to a relative mass constraint of 50 %. (c) The model is first meshed by 22,335 four-node tetrahedral 3D continuum elements (C3D4 [31]) having 6843 nodes and secondly, the model is meshed by 22,212 four-node tetrahedral 3D continuum elements (C3D4 [31]) having 6810 nodes. (d) A mesh comparison shows that the two meshes are generally rather similar.

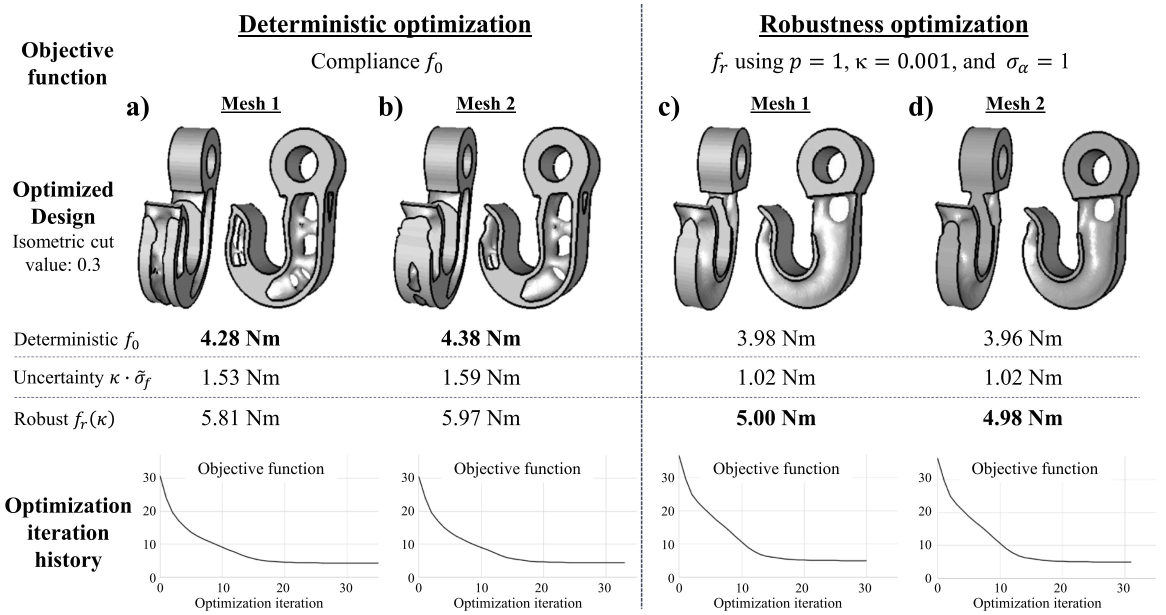

	a) Mesh 1	b) Mesh 2	c) Mesh 1	d) Mesh 2
Deterministic f_0	**4.28 Nm**	**4.38 Nm**	3.98 Nm	3.96 Nm
Uncertainty $\kappa \cdot \tilde{\sigma}_f$	1.53 Nm	1.59 Nm	1.02 Nm	1.02 Nm
Robust $f_r(\kappa)$	5.81 Nm	5.97 Nm	**5.00 Nm**	**4.98 Nm**

Fig. 13. Topology optimization results for the two models defined in Fig. 12. The deterministic topology optimization result for (a) mesh 1 and (b) mesh 2, respectively. The robust topology optimization result for (c) mesh 1 and (d) mesh 2 applying the novel sum uncertainty ($p = 1$) with $\sigma_\alpha = 1$ and $\kappa = 0.001$. Hence, the designs (a) and (b) have f_0 as the objective function compliance to be minimized whereas the designs (c) and (d) have f_r as the objective function compliance to be minimized. Additionally, the optimization iteration history of the objective function for all designs is shown.

Fig. 13a shows the deterministic topology optimization result for mesh 1 shown in Figs. 12c, and 13b shows the deterministic topology optimization result for mesh 2 shown in Fig. 12c. The two deterministic optimized designs have fundamentally different optimized material layouts in the designs, even though the differences in the two finite element meshes are very minor.

Fig. 13c shows the robust topology optimization result for mesh 1 and Fig. 13d shows the robust topology optimization result for mesh 2. The two robust optimized designs in Fig. 13c and d have numerically identical optimized material layouts and also have a significantly lower deterministic compliance f_0 than the two deterministic optimized designs in Fig. 13a and b, even though the robust optimized designs are optimized for the robust compliance f_r. Thus, the suppression of mesh-induced local minima and mesh-independence for the robust optimized designs is also shown for the given 3D continuum example.

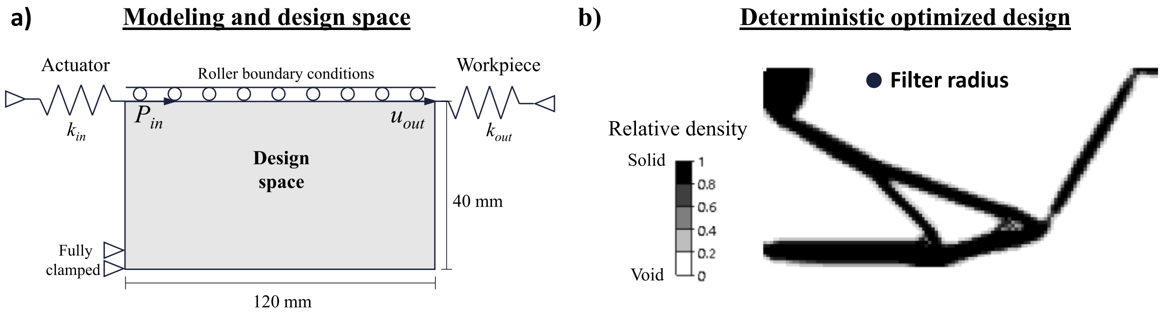

Fig. 14. Compliant topology optimization inverter mechanism benchmark example as defined in [8]. The design variable filter is applied for all mechanism examples and the design variable filter radius is the same for all optimization formulations. (a) The finite element model for the mechanism design has an input actuator defined using a linear spring $k_{in} = 1$ N/mm and a point load $P_{in} = 1$ N. The objective function is to minimize the output displacement u_{out} at the attachment point to a workpiece having the linear stiffness $k_{out} = 0.001$ N/mm. By minimizing the output displacement as objective function, an optimized inverter mechanism behavior is imposed. The design is subject to a relative mass constraint of 20 %. If not stated otherwise, then the model for the design space consists of 7200 four-node continuum plane stress elements (CPS4 [31]) having 7381 nodes. The material is modeled as linear elastic isotropic material with a Poisson's ratio of 0.3 and a Young's modulus of 1 MPa, and the filter radius is set to 2.5 mm. (b) Deterministic optimized design forming a hinge consisting of intermediate density elements being much smaller than the defined filter radius.

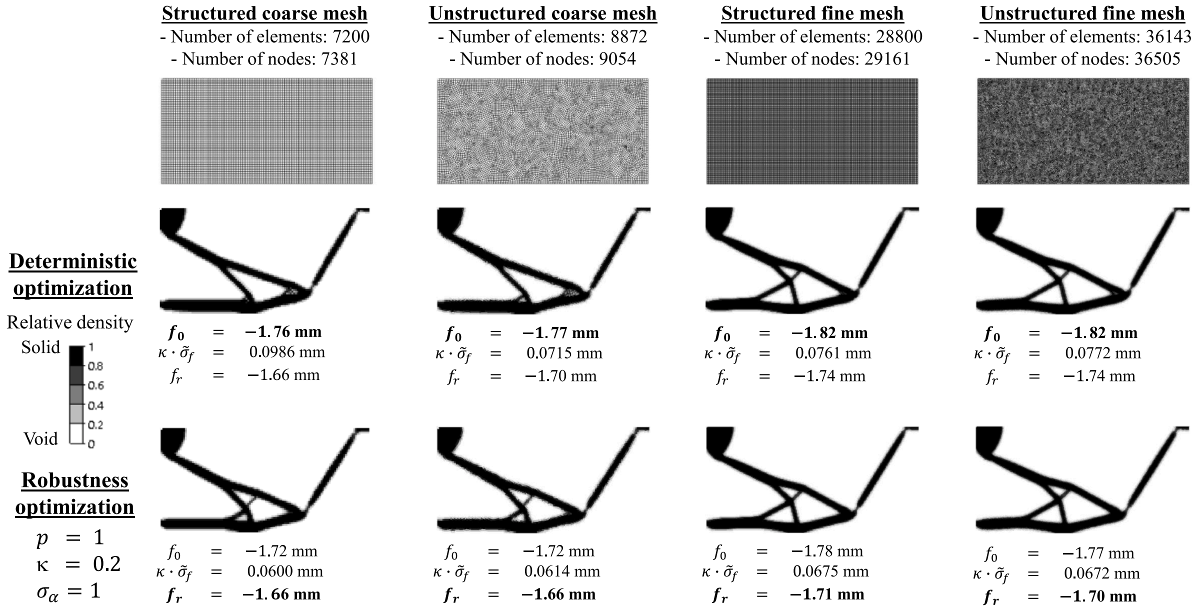

Fig. 15. Topology optimization results for the model defined in Fig. 14 using four different meshes being a structured coarse mesh, an unstructured coarse mesh, a structured fine mesh and an unstructured fine mesh, respectively. Two designs are determined for each mesh, one design being deterministically optimized and another design being robustly optimized ($p = 1$, $\kappa = 0.2$, $\sigma_\alpha = 1$). The design variable filter is applied where the filter radius is the same for all eight optimized designs.

5.3. Compliant force inverter

The compliant force inverter introduced in [8] and used as a benchmark example in [7] is defined in Fig. 14a. Fig. 14b shows the deterministic optimized design, featuring a compliant hinge that has a concentrated lumped region consisting of intermediate density elements, which is not feasible for manufacturing.

The nodal uncertainty contributions at the edges of the initial design space are not included in the calculation of the geometrical uncertainty to avoid singularity uncertainty contributions from the nodal boundary conditions and loading. Note, the design variable filter is applied, and the design variable filter radius is the same for all present optimized mechanism designs.

Fig. 15 shows the topology optimized mechanism using four different meshes being a structured coarse mesh, an unstructured coarse mesh, a structured fine mesh and an unstructured fine mesh, respectively. Two designs are determined for each mesh, one design being the deterministic optimized mechanism and another design being the robust optimized mechanism ($p = 1$, $\kappa = 0.2$, $\sigma_\alpha = 1$). The numerical results in Fig. 15 show that the four robust optimized mechanisms are similar in material layout, independent

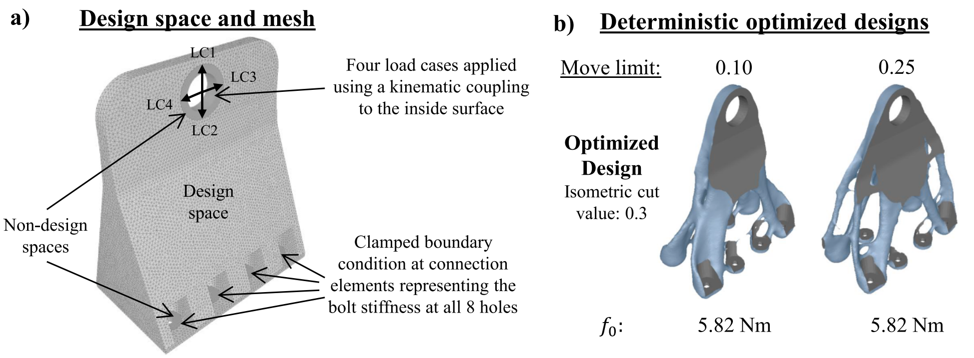

Fig. 16. (a) Design space, loads and boundary conditions, and optimization parameters for an aircraft bracket topology optimization. The total compliance of the four load cases (LC1 = 11.27 kN, LC2 = 11.27 kN, LC3 = 6.44 kN, and LC4 = 6.44 kN) is minimized as objective function subject to a relative mass constraint of 12.5 %. The model is meshed using 448,897 tetrahedral 3D continuum elements (C3D4 [31]) having 83,481 nodes. The material is modeled as linear elastic isotropic material with a Poisson's ratio of 0.33 and a Young's modulus of 68 GPa, and the filter radius is set to 1.3 times the characteristic element length. (b) The deterministic optimized designs using a move limit of the density design variable per optimization iteration of 0.25 and 0.10, respectively.

of the mesh, while the deterministic optimized mechanisms are significantly different for the two coarse meshes. One concludes that the robust optimization, including uncertainty for the geometrical uncorrelated nodal distributions in the optimization formulation, ensures a robust mechanism independent of acceptable changes in the finite element mesh and is thereby mesh-independent.

From the values of the deterministic response, it cannot be concluded that the obtained mesh-independent design is optimal in general or optimal for a specific mesh. This is due to length scale effects at the compliant hinges. No significant visual differences in the hinge design between the deterministic optimized mechanisms and the robust optimized mechanisms using $p = 1$ are observed. However, the compliance response is highly sensitive to even tiny differences in the geometric layout at the compliant hinge. Therefore, the impact of the present method on the compliant hinges is further investigated in Section 6.1 using larger values for the aggregation parameter p.

5.4. Aircraft bracket

The aircraft bracket is loaded at the top hole using four load cases and clamped at the bottom through eight bolt connections as shown in Fig. 16a. The compliance is minimized subject to a volume constraint of 12.5 % including the non-design areas around the top and bottom holes.

The deterministic optimized design is highly dependent on specific parameters of the optimization algorithm. In this study, only the so-called move limit of the Method of Moving Asymptotes [29] is varied where the move limit restricts the maximum allowable change of the design variable per optimization iteration. Fig. 16b shows the deterministic optimized designs using a move limit of 0.10 and 0.25, respectively. The optimized aircraft bracket designs are visualized using an isocut value of 0.3. The two deterministic designs are fundamentally different while having the same total compliance values. Note, the compliance for the different load cases is fundamentally different for both deterministic optimized designs.

Generally, to achieve numerical mesh-independence for the aforementioned examples, κ is chosen so that the weighted uncertainty measure is much smaller than the deterministic response value. However, for the present aircraft bracket suppression of local minima is not observed when choosing κ such that the weighted uncertainty measure has values similar to the deterministic compliance values of the optimized designs. Therefore, a numerical study is conducted in Fig. 17 using larger values for the weighting parameter κ.

Fig. 17 shows the robust optimized designs for two sets of move limit values and different κ values. All optimized designs in Fig. 17 are significantly different from their counterparts having either the same move limit value or the same κ value. All robust optimized designs in Fig. 17 for the applied move limit of 0.10 have higher deterministic compliance values compared to the deterministic optimized designs.

Applying the robust optimized designs as initial density distribution for a deterministic optimization yields optimized designs very similar to each applied initial density distribution. Additionally, the corresponding deterministic compliance values f_0 in Fig. 17 are very similar for the different density distributions. Therefore, we conclude that all obtained designs are local minima for a very flat region of the deterministic compliance.

Secondly, we conclude that the proposed method is not generally able to suppress local minima for the present application. The present differences are most likely caused by physical local minima, as discussed in Section 1, and cannot be addressed using the present robustness approach.

However, the deterministic optimized design in Fig. 17 obtained using a move limit of 0.25 is a mesh-induced local minimum. The best optimized design using the proposed method occurs at $\kappa = 0.1$ and differs significantly from the deterministic design. Furthermore,

Objective function	**Deterministic optimization**	**Robustness optimization**			
	Compliance f_0	f_r using $p = 1$ and $\sigma_\alpha = 1$			
	κ=0	κ=0.4	κ=1	κ=2	κ=3
Move limit 0.10: **Optimized Design** Isometric cut value: 0.3					
Deterministic f_0	**5.82 Nm**	5.82 Nm	5.90 Nm	5.93 Nm	5.97 Nm
Uncertainty $\tilde{\sigma}_f$	3.54 Nm	2.75 Nm	2.54 Nm	2.43 Nm	2.46 Nm
Robust $f_r(\kappa)$	5.82 Nm	**6.92 Nm**	**8.43 Nm**	**10.79 Nm**	**13.34 Nm**
Deterministic f_0 using optimized design as initial Φ	5.82 Nm	5.82 Nm	5.83 Nm	5.83 Nm	5.80 Nm
Move limit 0.25: **Optimized Design** Isometric cut value: 0.3				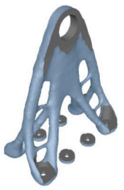	
Deterministic f_0	**5.82 Nm**	5.73 Nm	5.67 Nm	5.73 Nm	5.88 Nm
Uncertainty $\tilde{\sigma}_f$	3.78 Nm	2.85 Nm	2.58 Nm	2.44 Nm	2.43 Nm
Robust $f_r(\kappa)$	5.82 Nm	**6.87 Nm**	**8.25 Nm**	**10.60 Nm**	**13.17 Nm**
Deterministic f_0 using optimized design as initial Φ	5.82 Nm	5.69 Nm	5.63 Nm	5.65 Nm	5.70 Nm

Fig. 17. Robust topology optimization results for the model defined in Fig. 16 using different values for the weighting factor κ. Note, $\kappa = 0$ yields the deterministic optimized design and different move limits of 0.10 and 0.25 are applied, respectively. Additionally, the second deterministic f_0 is the optimized compliance for a deterministic optimization using each robust optimized design as the initial density distribution. Even though the compliance improves, which is expected due to the relaxation of the objective function ($\kappa = 0$), visually almost no difference is observable. Hence, the deterministic optimized designs are not depicted.

increasing κ, as shown in Fig. 17, leads to the suppression of small design features and slightly more symmetric optimized designs are obtained for only very minor increases in the compliance values.

6. Numerical results for physical robustness

This section studies the influence of using larger values for the aggregation parameter p. This provides an understanding of the intended numerical mesh-independence for $p = 1$ and the standard deviation for $p = 2$. Two additional studies are enhanced hinge designing for the compliant mechanism shown in Section 6.1 and compliance optimization in Section 6.2 yielding designs similar to stress-constrained optimized designs. The L^p-norm approximates the L^∞-norm for large values of p. Hence, only the nodes having the largest geometrical standard deviations influence the optimized designs.

Single-node hinges and stress singularities can be viewed as inadequacies of the numerical modeling. However, they are also classified as physical robustness since the optimized designs are very sensitive regarding their physical realization and manufacturing at certain locations of the designs.

6.1. Compliant force inverter

Section 5.3 concludes that the proposed method affects the hinge design due to large nodal standard deviations at the so-called compliant hinges. Therefore, the same example is investigated using larger values for the aggregation parameter p, which thereby yields a very localized uncertainty measure at the compliant hinges.

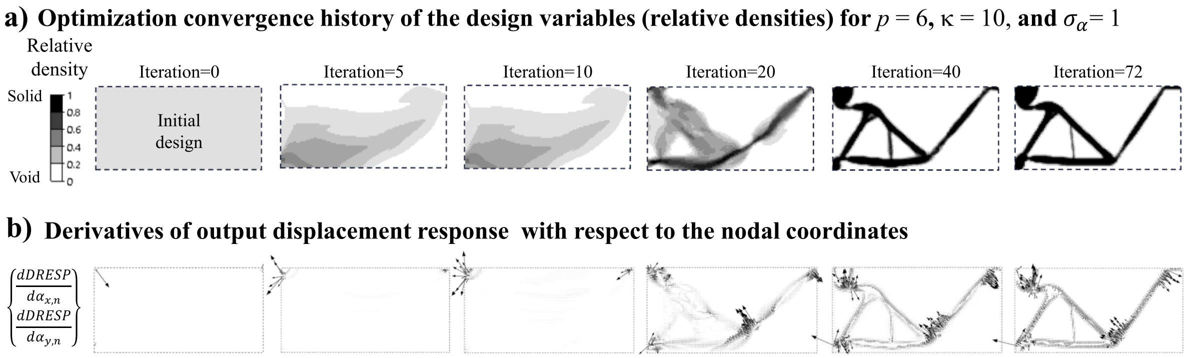

Fig. 18. Optimization iteration history for (a) the design variables (relative densities) and (b) the nodal standard deviation, which is the magnitude of $df/d\tilde{\alpha}_n$ for optimization iterations 0, 5, 10, 20, 40 and 72 using the novel uncertainty ($p = 6$) for $\kappa = 10$ and $\sigma_\alpha = 1$ for the output displacement u_{out} as the objective function to be minimized, defined in Fig. 14.

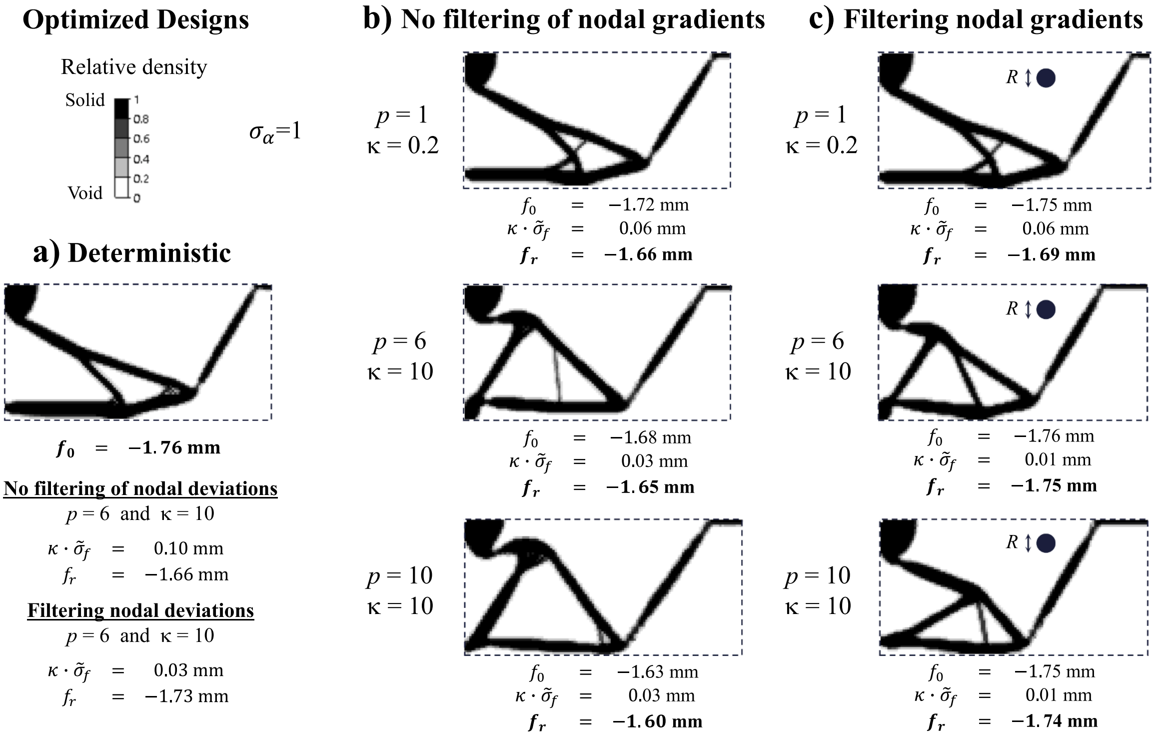

Fig. 19. Topology optimization result of the model defined in Fig. 14 for (a) the deterministic optimization solution, (b) the robust optimization results for no filtering of nodal gradients and (c) the robust optimization results for the filtering of nodal gradients using the radius R. The robust optimized designs are obtained for ($p = 1$, $\kappa = 0.2$, $\sigma_\alpha = 1$), ($p = 6$, $\kappa = 10$, $\sigma_\alpha = 1$) and ($p = 10$, $\kappa = 10$, $\sigma_\alpha = 1$), respectively. The design variable filter is applied, and the corresponding design variable filter radius is the same for all seven optimized designs.

Fig. 18a shows the optimization iteration history for the design variables using the novel uncertainty for $p = 6$, $\kappa = 10$, and $\sigma_\alpha = 1$ where the objective function f_r is minimized. Fig. 18b shows the vector of the nodal standard deviations for optimization iteration 0, 5, 10, 20, 40 and 72, respectively.

Firstly, Fig. 18b shows that the uncertainty measure $\tilde{\sigma}_f$ changes significantly during the optimization iterations. Secondly, the locations of the nodal standard deviations contributing the most to the overall $\tilde{\sigma}_f$, change their locations fundamentally during the optimization iterations. Thirdly, Fig. 18b also shows that the largest nodal standard deviations for the last optimization iterations are located at the so-called compliant hinges. Thus, the proposed method considering uncorrelated nodal distributions is an alternative approach to design compliant hinges in topology optimization for compliant mechanisms.

The optimization results in Figs. 19 and 20 show the influence of the parameters for the geometrical uncertainty approach on the so-called hinges in compliant mechanism design. Fig. 19a shows the deterministic optimization solution, Fig. 19b shows the robust

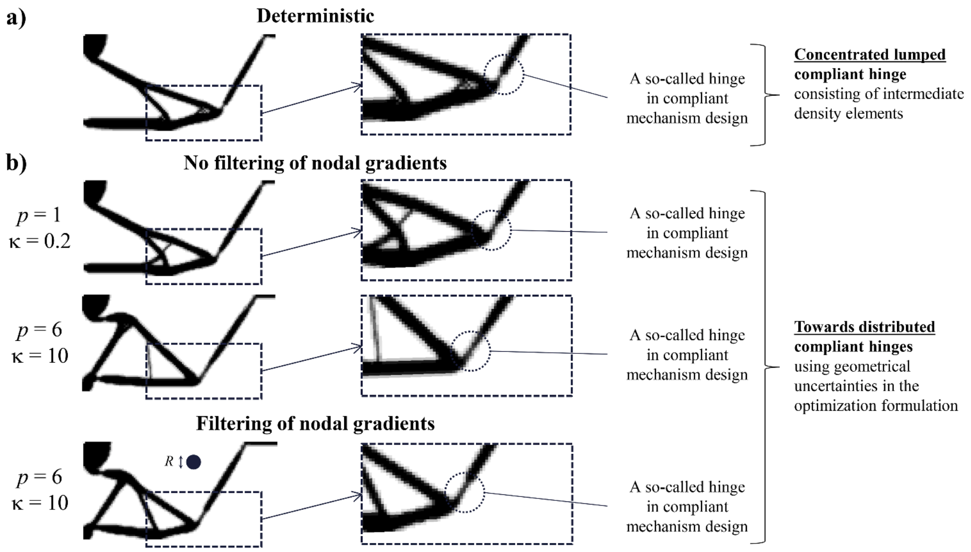

Fig. 20. (a) The deterministic optimized compliant mechanism design has a compliant hinge consisting of a concentrated lumped region having intermediate density elements. Several procedures indirectly suppress the concentrated lumped regions with intermediate density elements to mimic a compliant hinge. (b) The proposed approach for uncertainties using geometrical uncorrelated nodal distributions introduces a method that pushes the material layout for the optimized mechanism designs towards distributed compliant hinges.

optimization results applying no filtering of the nodal gradients, and Fig. 19c shows the robust optimization results applying filtering of the nodal gradients using the radius R. The three robust optimized designs are obtained for ($p = 1$, $\kappa = 0.2$, $\sigma_\alpha = 1$), ($p = 6$, $\kappa = 10$, $\sigma_\alpha = 1$) and ($p = 10$, $\kappa = 10$, $\sigma_\alpha = 1$), respectively.

Fig. 20a shows that the deterministic compliant mechanism design has a compliant hinge consisting of a concentrated lumped region, which contains intermediate density elements. This approach for uncertainties using geometrical nodal uncorrelated distributions introduces a method that pushes the optimized mechanism designs towards distributed compliant hinges, improving feasibility for manufacturing.

The robust optimized designs in Fig. 20b also show that applying a higher exponent $p = 6$ or including filtering of the nodal gradients enforces a larger distribution of the compliant hinges compared to applying the exponent $p = 1$ and no filtering of the nodal gradients.

Consequently, the robust optimization formulation using the uncertainty measure for geometrically uncorrelated nodal distributions can also be applied to constructively impact the physical design so that the physical designing is less sensitive to very localized geometrical distributions, e.g., for manufacturing considerations. Thus, a geometrical robust design with respect to the most sensitive locations for manufacturing is obtained.

6.2. Norwegian sock

The L-shape beam, also called Norwegian sock, is defined in Fig. 21a. Due to the stress singularity at the inner corner, the L-shape beam is frequently studied in topology optimization literature. Fig. 21 shows the deterministic optimized designs for a mass minimization as objective function subject to a stress constraint and a compliance minimization as objective function subject to a mass constraint having the same mass as the stress-constrained design. The two optimized designs differ significantly since the compliance-minimized design has a stress singularity at the inner corner.

Note, a move limit of 0.10 is imposed on the relative density design variable, and a density filter having the same filter radius is applied for all optimized designs.

The deterministic optimization results are also shown in Fig. 22a and b. As expected, the compliance optimized design in Fig. 22b has a lower compliance value at the cost of having a two times larger stress value. In contrast, the robust compliance-optimized designs in Fig. 22c and d using $p = 5$, $\kappa = 1$, and $\sigma_\alpha = 1$ with and without filtering of the nodal gradients are more similar to the stress-constrained optimized designs than to the deterministic compliance optimized designs and do not contain the inner sharp corner causing the high stress singularity for the deterministic stiffness optimized design. Additionally, the stress response values are significantly reduced for the two robust compliance optimized designs. Fig. 22d shows the robust optimized design, where the nodal gradients are filtered characterized by the filter radius R and numerically the stress response and the mass have the same values as for the stress-constrained design in Fig. 22a but a significantly improved compliance response is obtained compared to the strength optimized design in Fig. 22a.

We conclude that the proposed method using large values of p implicitly minimizes the stress peaks at the cost of a slightly larger deterministic compliance. However, choosing the weighting factor κ is not straightforward when a specific threshold for the stresses

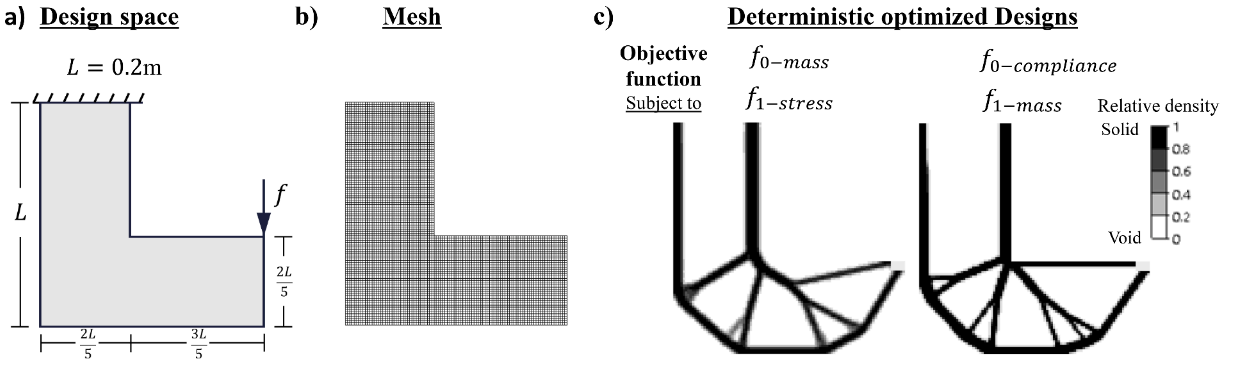

Fig. 21. (a) Design space, loading $f = 1.5$ kN and boundary conditions for an L-shape beam. The material is modeled as linear elastic isotropic material with a Poisson's ratio of 0.33, a Young's modulus of 71 MPa, and a density of 1 kg/m^3. The depth is 1 mm and the filter radius is set to 2.6 mm.(b) The model for the design space consists of 6400 four-node continuum plane stress elements (CPS4 [31]) and 6601 nodes. (c) Deterministic optimized designs for mass minimization subject to a stress constraint of 600 Mpa and a compliance minimization subject to a mass constraint having the same mass as the mass of the stress-constrained optimized design.

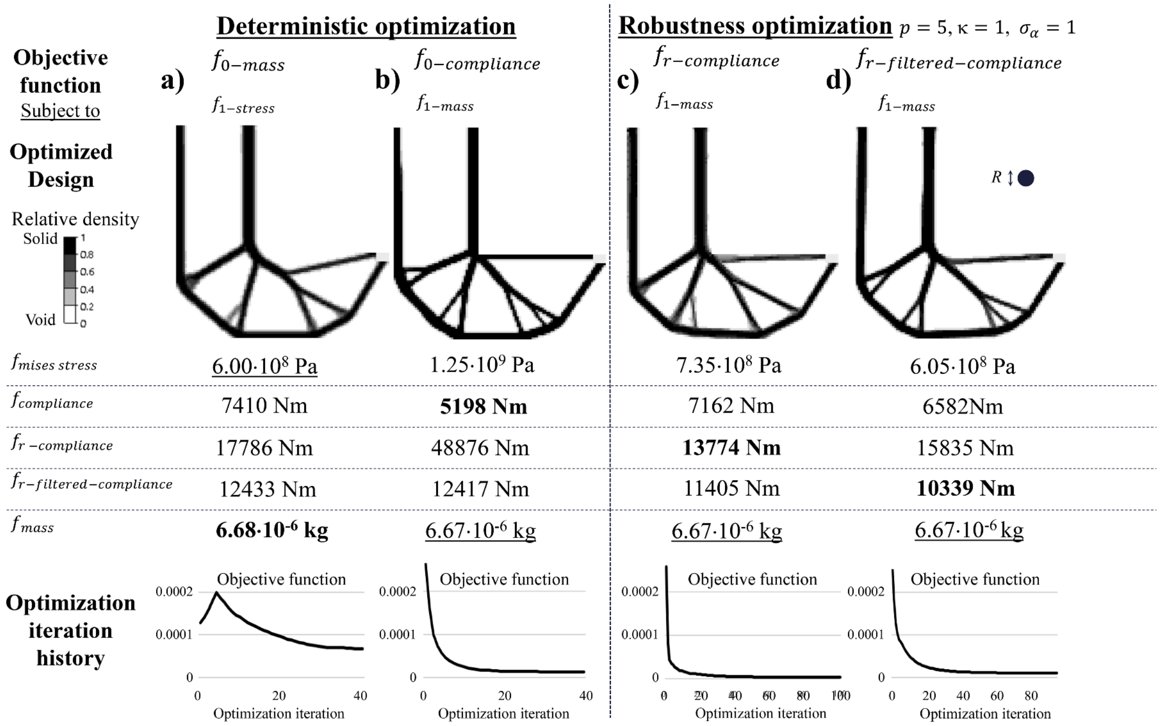

	a) f_{0-mass} / $f_{1-stress}$	b) $f_{0-compliance}$ / f_{1-mass}	c) $f_{r-compliance}$ / f_{1-mass}	d) $f_{r-filtered-compliance}$ / f_{1-mass}
$f_{mises\ stress}$	$6.00 \cdot 10^8$ Pa	$1.25 \cdot 10^9$ Pa	$7.35 \cdot 10^8$ Pa	$6.05 \cdot 10^8$ Pa
$f_{compliance}$	7410 Nm	**5198 Nm**	7162 Nm	6582Nm
$f_{r-compliance}$	17786 Nm	48876 Nm	**13774 Nm**	15835 Nm
$f_{r-filtered-compliance}$	12433 Nm	12417 Nm	11405 Nm	**10339 Nm**
f_{mass}	**$6.68 \cdot 10^{-6}$ kg**	$6.67 \cdot 10^{-6}$ kg	$6.67 \cdot 10^{-6}$ kg	$6.67 \cdot 10^{-6}$ kg

Fig. 22. Topology optimization results for the L-beam model defined in Fig. 21. The deterministic optimized design for (a) a mass minimization subject to a stress constraint and (b) a compliance minimization subject to a mass constraint. The (c) robust topology optimization result and the (d) robust optimization result using filtering of the nodal gradients with the filter radius R using $\sigma_\alpha = 1$, $\kappa = 1$, and $p = 5$. Hence, the designs (a) and (b) have f_0 as the objective function to be minimized whereas the design (c) has f_r and (d) has $f_{robust-filtered}$ as the objective function to be minimized. Additionally, the optimization iteration history of the objective functions for all designs are shown. The density filter radius is the same for all optimizations. Additionally, a move limit of 0.1 per optimization iteration is imposed on the normalized density variable.

should be fulfilled. Additionally, the filtering of the nodal gradients improves the convergence in comparison to the unfiltered robust optimization. Though, the robust stiffness optimized designs require about twice as many optimization iterations as the deterministic optimized solutions, compared to both the stiffness and the strength optimization.

7. Recommended parameter values for geometrical uncertainty scheme

Based on the present numerical studies, we recommend the following numerical values for the parameters κ in (2) and $\hat{\epsilon}$ in (17):

- $\kappa = 0.1 \cdot \dfrac{\mu_f}{\tilde{\sigma}_f}$ of the design of the initial optimization iteration (for $p = 1$ and $\sigma_\alpha = 1$)
- $\hat{\epsilon}$ = characteristic element length $\cdot\, 10^{-2}$

8. Conclusion

This study presents a novel isotropic geometrical uncertainty measure based on the L^p-norm aggregation of the nodal uncorrelated standard deviations. For $p = 1$, the measure is mesh-independent and effectively suppresses mesh-induced local minima for the optimized designs. For higher values of p, the method diminishes the impact of localized geometric variation, resembling the characteristics of stress-constrained optimized designs and contributing constructively to enforcing the desired length scale for hinge designing in compliant mechanisms. A semi-intrusive and computationally efficient first-order principal sensitivity approach is implemented to compute the required sensitivities of the geometrical uncertainty measure which requires only one additional finite element analysis per optimization iteration for continuum models and two additional finite element analyses per optimization iteration for shell models.

Note, the selected numerical examples, featuring symmetric design domains, straightforward loading configurations, and linear finite element models, are intentionally chosen due to their demonstrated susceptibility to mesh-induced local minima. While the proposed method proves effective in these scenarios, further studies should explore broader modeling approaches and alternative objective functions that may inherently suppress such numerical artifacts.

CRediT authorship contribution statement

Justus Karnath: Writing – review & editing, Writing – original draft, Visualization, Software, Methodology, Investigation, Conceptualization; **Benedikt Kriegesmann:** Writing – review & editing, Methodology, Conceptualization; **Claus B.W. Pedersen:** Writing – review & editing, Writing – original draft, Methodology, Conceptualization.

Data availability

Data, models and code is provided on reasonable request.

Declaration of competing interest

The authors state that there are no conflict of interest.

Acknowledgment

This research did not receive any specific grant from funding agencies in the public, commercial, or not-for-profit sectors.

Appendix A. Theory and implementation details for the L^p-norm-based geometrical uncertainty measure

These present appendices provide additional theoretical and implementation details for the proposed robustness method.

A.1. Minimum thresholding for geometrical uncertainty measure calculation and corresponding sensitivities

The geometrical perturbation field $\Delta\boldsymbol{\alpha}$ in (16) for $p = 1$ has numerical issues when $\left\|\frac{df_\mu}{d\hat{\alpha}_n}\right\|_2$ approximates zero as the denominator (as shown in Fig. 5b) approaches zero (division by numerical zero) and the geometrical perturbation field vector $\Delta\boldsymbol{\alpha}$ will then have large numerical values. Therefore, a threshold scheme is applied to suppress the devision by numerical zero for determining the uncertainty measure $\tilde{\sigma}_f$ and the corresponding sensitivities. Initially, the threshold scheme determines the maximum nodal standard deviation over all nodal contributions. Afterward, only the nodal standard deviations having a value higher than a certain fraction β of the maximum nodal standard deviation are included in determining the uncertainty measure $\tilde{\sigma}_f$ and the geometrical perturbation field $\Delta\boldsymbol{\alpha}$ as

$$\sigma_{f,n} = \begin{cases} \sigma_{f,n}, & \text{if } \sigma_{f,n} \geq \beta \cdot \max_i(\sigma_{f,i}) \\ 0, & \text{otherwise} \end{cases}. \tag{A.1}$$

The threshold parameter β is set to 0.01 in all present studies and is only applied for shell models when optimizing using the aggregation parameter $p = 1$. Numerical studies show that the values for the geometrical uncertainty measure $\tilde{\sigma}_f$ hardly change compared to not applying the threshold scheme.

A.2. Normalization for L^p-norm aggregation

A normalization of the aggregated nodal standard deviations is required to prevent numerical overflows in the numerical implementation when choosing large values of p for the aggregation function. Therefore, the largest value of the nodal standard deviation $\sigma_{\max}$ is used to normalize the terms being penalized by the power of p yielding

$$\tilde{\sigma} = \sigma_{\max}\left(\sum_{n=1}^{N}\left(\frac{\sigma_{f,n}}{\sigma_{\max}}\right)^{p}\right)^{\frac{1}{p}} \quad \text{, where} \quad \sigma_{\max} = \max_i(\sigma_{f,i}). \tag{A.2}$$

Thereby, the corresponding geometrical perturbation $\Delta\hat{\boldsymbol{\alpha}}_n$ for the gradient calculation reads

$$\Delta\hat{\boldsymbol{\alpha}}_n = \frac{1}{\left(\sum_{n=1}^{N}\left(\frac{\sigma_{f,n}}{\sigma_{\max}}\right)^{p}\right)^{\frac{p-1}{p}}}\left(\frac{\sigma_{f,n}}{\sigma_{\max}}\right)^{p-2}\frac{\left(\frac{df_{\boldsymbol{\mu}}}{d\alpha_{x,n}}, \frac{df_{\boldsymbol{\mu}}}{d\alpha_{y,n}}, \frac{df_{\boldsymbol{\mu}}}{d\alpha_{z,n}}\right)^{\mathrm{T}}}{\sigma_{\max}}. \tag{A.3}$$

A.3. Filtering of the nodal gradients

A linear filter can be applied on the nodal gradient $df/d\boldsymbol{\alpha}$ for additional regularization. Since the entries of the nodal gradient are not strictly positive then classical filtering allows for cancellation causing additional local minima. Hence, nodal filtering is applied as a scaling of the magnitude of the nodal gradient $df/d\hat{\boldsymbol{\alpha}}_n$, while maintaining the direction of the gradient and reads as follows:

$$\frac{d\bar{f}}{d\hat{\boldsymbol{\alpha}}_n} = \frac{1}{\sum_{i=1}^{N} H_i}\sum_{i=1}^{N} H_i\left|\frac{df}{d\hat{\boldsymbol{\alpha}}_i}\right|_2 \frac{\frac{df}{d\hat{\boldsymbol{\alpha}}_n}}{\left|\frac{df}{d\hat{\boldsymbol{\alpha}}_n}\right|_2}, \tag{A.4}$$

where the weighting function H_i is given by the linear decaying cone shape function and defined as

$$H_i = \begin{cases} \frac{R-r_i}{R}, & \text{if } r_i < R \\ 0, & \text{otherwise} \end{cases}, \tag{A.5}$$

where R is the filter radius and $r_i = ||\hat{\boldsymbol{\alpha}}_i - \hat{\boldsymbol{\alpha}}_n||_2$ the distance between any pair of nodes.

For $p = 1$, the present filtering of nodal gradients has no practical effect other than a linear scaling of the uncertainty measure as the gradient direction is not affected since only the direction of $\frac{df_{\boldsymbol{\mu}}}{d\boldsymbol{\alpha}}$ is applied as perturbation for the gradient computation. Hence, the proposed nodal filtering of the gradients is only applied in Section 6 for $p > 1$ and yields improved convergence toward a solid-void design.

Appendix B. Theory and implementation details for shell models

The present appendices investigates the application of the proposed method for shell models.

B.1. In-plane projection

When applying the present geometrical uncertainty measure to shell elements, then the nodal gradients $df_{\boldsymbol{\mu}}/d\hat{\boldsymbol{\alpha}}_n$ are projected onto the plane of the shell element using each nodal normal direction $\boldsymbol{n}$

$$\frac{df_{\boldsymbol{\mu}}}{d\hat{\boldsymbol{\alpha}}}_{in-plane} = \frac{df_{\boldsymbol{\mu}}}{d\hat{\boldsymbol{\alpha}}} - \boldsymbol{n}^{\mathrm{T}}\frac{df_{\boldsymbol{\mu}}}{d\hat{\boldsymbol{\alpha}}}\boldsymbol{n}. \tag{B.1}$$

The projection has the same effect as directly defining the random variables using a coordinate system strictly defined in the plane of the shell element. Thus, the underlying mesh uncertainty is modeled more precisely with respect to typical procedures applied for the shell mesh generation.

B.2. Finite difference approach implementation

The sensitivity equation in (16) can be seen as forward (or backward) numerical finite difference sensitivity approach; see [34]. Thus, the numerical sensitivity equation can also be modified to a central finite difference approach [34] as

$$\frac{d\tilde{\sigma}_f}{d\boldsymbol{\phi}} = \frac{d^2 f}{d\boldsymbol{\phi}\, d\boldsymbol{\alpha}}(\boldsymbol{\mu}_{\alpha})\Delta\boldsymbol{\alpha} \approx \frac{1}{2\epsilon}\left[\frac{df}{d\boldsymbol{\phi}}\left(\boldsymbol{\mu}_{\alpha} + \epsilon\Delta\boldsymbol{\alpha}\right) - \frac{df}{d\boldsymbol{\phi}}\left(\boldsymbol{\mu}_{\alpha} - \epsilon\Delta\boldsymbol{\alpha}\right)\right]. \tag{B.2}$$

Generally, the central finite difference approach is numerically more accurate in the sensitivity calculations than the forward (or backward) finite difference approach, but the central finite difference approach has twice the computational cost than the forward (or backward) finite difference approach. Therefore, the finite difference approach for the sensitivities is specifically examined in Fig. B.1 using four 2D plane stress continuum elements (CPS4 [31]) and for four 3D shell elements (S4 [31]), respectively.

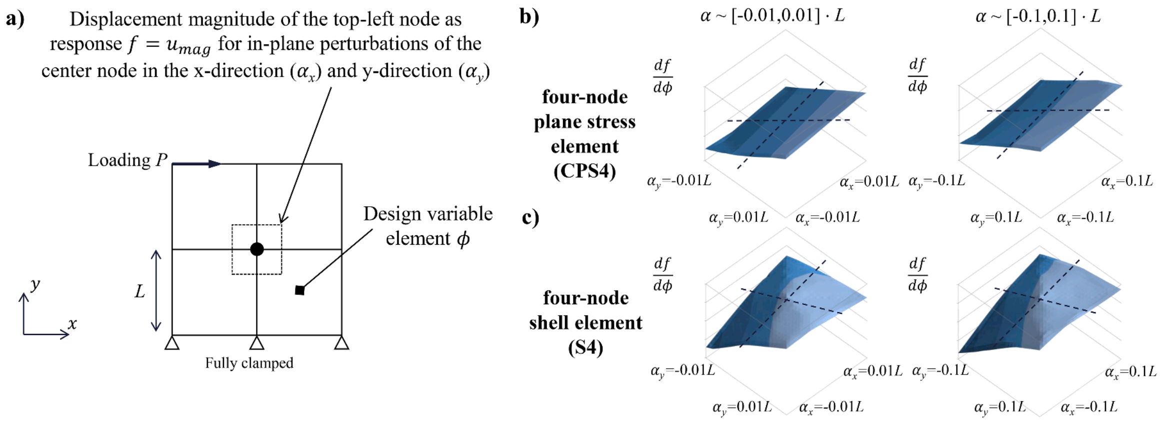

Fig. B.1. (a) The variation of the sensitivity $df/d\phi$ for the in-plane geometrical perturbations α_x and α_y in the x-direction and y-direction of the center node representing the geometrical perturbation field $\Delta\boldsymbol{\alpha}$. The variation of the sensitivity $df/d\phi$ for the geometrical perturbations α_x and α_y using (b) a four-node plane stress element (CPS4 [31]) and using (c) a four-node shell element (S4 [31]), respectively. The results show that the forward (or backward) finite difference approach is sufficient for the 2D continuum element model (b) whereas the results in (c) demonstrate that the computational more costly central finite difference approach is required for the 3D shell element model.

The in-plane geometrical perturbations in the x-direction α_x and y-direction α_y of the center node in Fig. B.1a represent the geometrical perturbation field $\Delta\boldsymbol{\alpha}$. The displacement magnitude u_{mag} at the loading point P is the response $f = u_{mag}$ for which the topology sensitivity $df_\mu/d\phi$ is calculated for the element shown in Fig. B.1a. Fig. B.1b and c show the sensitivity $df/d\phi$ variation for the geometrical perturbations α_x and α_y of the four-node plane stress model and the four-node shell model, respectively. Fig. B.1b demonstrates that a forward (or backward) finite difference approach is sufficient for the 2D continuum element model, while Fig. B.1c demonstrates that the computationally more costly central finite difference approach is required to obtain acceptable numerical accuracy for the 3D shell element model.

Consequently, several numerical experiments verified that for all element types having only translational degrees of freedom (e.g., 2D and 3D continuum elements) then the forward finite difference approach is sufficient. For all element types having both translational and rotational degrees of freedom (e.g., shell and beam elements) then the central finite difference approach should be applied.

References

[1] O. Sigmund, J. Petersson, Numerical instabilities in topology optimization: a survey on procedures dealing with checkerboards, mesh-dependencies and local minima, Struct. Optim. 16 (1) (1998) 68–75. https://doi.org/10.1007/BF01214002

[2] I.P.A. Papadopoulos, P.E. Farrell, T.M. Surowiec, Computing multiple solutions of topology optimization problems, SIAM J. Sci. Comput. 43 (3) (2021) A1555–A1582. https://doi.org/10.1137/20M1326209

[3] C. Talischi, G.H. Paulino, A. Pereira, I.F.M. Menezes, Polygonal finite elements for topology optimization: a unifying paradigm, Int. J. Numer. Methods Eng. 82 (6) (2010) 671–698. https://doi.org/10.1002/nme.2763

[4] P.F. Antonietti, M. Bruggi, S. Scacchi, M. Verani, On the virtual element method for topology optimization on polygonal meshes: a numerical study, Comput. Math. Appl. 74 (5) (2017) 1091–1109. https://doi.org/10.1016/j.camwa.2017.05.025

[5] O. Sigmund, K. Maute, Topology optimization approaches: a comparative review, Struct. Multidiscip. Optim. 48 (6) (2013) 1031–1055. https://doi.org/10.1007/s00158-013-0978-6

[6] B.S. Lazarov, F. Wang, O. Sigmund, Length scale and manufacturability in density-based topology optimization, Arch. Appl. Mech. 86 (1) (2016) 189–218. https://doi.org/10.1007/s00419-015-1106-4

[7] O. Sigmund, Morphology-based black and white filters for topology optimization, Struct. Multidiscip. Optim. 33 (4–5) (2007) 401–424. https://doi.org/10.1007/s00158-006-0087-x

[8] O. Sigmund, On the design of compliant mechanisms using topology optimization, Mech. Struct. Mach. 25 (4) (1997) 493–524. Publisher: Taylor & Francis, https://doi.org/10.1080/08905459708945415

[9] A.D. Kiureghian, O. Ditlevsen, Aleatory or epistemic? Does it matter?, Struct. Saf. 31 (2) (2009) 105–112. https://doi.org/10.1016/j.strusafe.2008.06.020

[10] K. Steltner, B. Kriegesmann, C.B.W. Pedersen, Robust sizing optimization of stiffened panels subject to geometric imperfections using fully nonlinear postbuckling analyses, Thin Wall. Struct. 175 (2022) 109195. https://doi.org/10.1016/j.tws.2022.109195

[11] A. Haldar, S. Mahadevan, Probability, Reliability and Statistical Methods in Engineering Design, John Wiley & Sons, New York ; Chichester England, 1. auflage edition, New York ; Chichester England, 1999.

[12] M. Schevenels, B.S. Lazarov, O. Sigmund, Robust topology optimization accounting for spatially varying manufacturing errors, Comput. Methods Appl. Mech. Eng. 200 (49–52) (2011) 3613–3627. https://doi.org/10.1016/j.cma.2011.08.006

[13] B. Sudret, S. Marelli, J. Wiart, Surrogate models for uncertainty quantification: an overview, in: 2017 11th European Conference on Antennas and Propagation (EUCAP), 2017, pp. 793–797. ISSN: null. https://doi.org/10.23919/EuCAP.2017.7928679

[14] I. Doltsinis, Z. Kang, Robust design of structures using optimization methods, Comput. Methods Appl. Mech. Eng. 193 (23) (2004) 2221–2237. https://doi.org/10.1016/j.cma.2003.12.055

[15] I. Doltsinis, Z. Kang, G. Cheng, Robust design of non-linear structures using optimization methods, Comput. Methods Appl. Mech. Eng. 194 (12) (2005) 1779–1795. https://doi.org/10.1016/j.cma.2004.02.027

[16] B.S. Lazarov, M. Schevenels, O. Sigmund, Topology optimization considering material and geometric uncertainties using stochastic collocation methods, Struct. Multidiscip. Optim. 46 (4) (2012) 597–612. https://doi.org/10.1007/s00158-012-0791-7

[17] M. Kranz, J.K. Lüdeker, B. Kriegesmann, A generalized approach for robust topology optimization using the first-order second-moment method for arbitrary response functions, Struct. Multidiscip. Optim. 66 (5) (2023) 98. https://doi.org/10.1007/s00158-023-03540-w

[18] M. Jansen, G. Lombaert, M. Schevenels, Robust topology optimization of structures with imperfect geometry based on geometric nonlinear analysis, Comput. Methods Appl. Mech. Eng. 285 (2015) 452–467. https://doi.org/10.1016/j.cma.2014.11.028

[19] J.C. Krüger, B. Kriegesmann, Efficient robust topology optimization of eigenfrequencies using the first-order second-moment method, in: K. Nachbagauer, A. Held (Eds.), Optimal Design and Control of Multibody Systems, IUTAM Bookseries, Springer Nature Switzerland, Cham, 2024, pp. 75–84. https://doi.org/10.1007/978-3-031-50000-8_7

[20] K. Steltner, C.B.W. Pedersen, B. Kriegesmann, Semi-intrusive approach for stiffness and strength topology optimization under uncertainty, Optim. Eng. (2022). https://doi.org/10.1007/s11081-022-09770-z

[21] J.C. Krüger, M. Kranz, T. Schmidt, R. Seifried, B. Kriegesmann, An efficient and non-intrusive approach for robust design optimization with the first-order second-moment method, Comput. Methods Appl. Mech. Eng. 414 (2023) 116136. https://doi.org/10.1016/j.cma.2023.116136

[22] I. Ben-Yelun, A.O. Yuksel, F. Cirak, Robust topology optimisation of lattice structures with spatially correlated uncertainties, Struct. Multidiscip. Optim. 67 (2) (2024) 16. https://doi.org/10.1007/s00158-023-03716-4

[23] M. Jansen, G. Lombaert, M. Diehl, B.S. Lazarov, O. Sigmund, M. Schevenels, Robust topology optimization accounting for misplacement of material, Struct. Multidiscip. Optim. 47 (3) (2013) 317–333. https://doi.org/10.1007/s00158-012-0835-z

[24] J.K. Guest, T. Igusa, Structural optimization under uncertain loads and nodal locations, Comput. Methods Appl. Mech. Eng. 198 (1) (2008) 116–124. https://doi.org/10.1016/j.cma.2008.04.009

[25] B. Sudret, A. Der Kiureghian, Stochastic Finite Element Methods and Reliability: A State-of-the-Art Report, Technical Report UCB/SEMM-2000/08, Department of Civil and Environmental Engineering, University of California Berkeley, Berkeley, California, 2000.

[26] M.P. Bendsøe, Optimal shape design as a material distribution problem, Struct. Optim. 1 (4) (1989) 193–202. https://doi.org/10.1007/BF01650949

[27] O. Sigmund, K. Maute, Sensitivity filtering from a continuum mechanics perspective, Struct. Multidiscip. Optim. 46 (4) (2012) 471–475. https://doi.org/10.1007/s00158-012-0814-4

[28] K. Svanberg, H. Svärd, Density filters for topology optimization based on the pythagorean means, Struct. Multidiscip. Optim. 48 (5) (2013) 859–875. https://doi.org/10.1007/s00158-013-0938-1

[29] K. Svanberg, The method of moving asymptotes - a new method for structural optimization, Int. J. Numer. Methods Eng. 24 (2) (1987) 359–373. https://doi.org/10.1002/nme.1620240207

[30] B. Kriegesmann, J.K. Lüdeker, Robust compliance topology optimization using the first-order second-moment method, Struct. Multidiscip. Optim. 60 (1) (2019) 269–286. https://doi.org/10.1007/s00158-019-02216-8

[31] Simulia, Abaqus, Dassault Systèmes, 2024.

[32] Y. Kanno, On three concepts in robust design optimization: absolute robustness, relative robustness, and less variance, Struct. Multidiscip. Optim. 62 (2) (2020) 979–1000. https://doi.org/10.1007/s00158-020-02503-9

[33] Simulia, Tosca Structure, Dassault Systèmes, 2024.

[34] D.A. Tortorelli, P. Michaleris, Design sensitivity analysis: overview and review, Inverse Prob. Eng. 1 (1) (1994) 71–105. https://doi.org/10.1080/174159794088027573